Evaluation of Dynamically Downscaled Simulations

7

Authors:

Venkatraman Prasanna, Aurel Florian Moise, Sandeep Sahany, Muhammad Eeqmal Hassim, Chen Chen, Xin Rong Chua, Gerald Lim, Shipra Jain, Jianjun Yu, Pavan Harika Raavi, Fei Luo

METEOROLOGICAL SERVICE SINGAPORE
Centre for Climate Research Singapore

7.1 Introduction

This chapter presents the evaluation of the 8km and 2km dynamically downscaled historical simulations against observations (both in-situ and remotely sensed) and reanalysis (gridded proxy for observations) data. Six CMIP6 GCMs have been dynamically downscaled to 8 km resolution for the historical period (1955-2014), and five out of the six 8km downscaled simulations have been further downscaled to 2 km resolution for the period 1995-2014. For details on the downscaled simulations please refer to Chapter 6.

As a part of the evaluation of the dynamically downscaled historical simulations we present the assessment of:

(1) Large-scale consistency between the driving GCM and the resulting downscaled simulations - as a result of dynamical downscaling, although we expect the downscaled simulations to capture the finer spatial scale features of rainfall, temperature, etc. due to improved representation of coastlines, mountains and land-use-land-cover we also expect the simulations to have large-scale consistency with the driving GCM.

(2) Regional (Southeast Asia and Western Maritime Continent) and local (Singapore) climatology (rainfall, temperature, humidity and winds) – it is important to know which aspects of the regional and local climatology are captured well in the downscaled simulations and which aspects are not in order to use the future projections in a more informed manner both for physical climate change assessment and climate impacts modeling.

(3) Key regional climate drivers (northeast monsoon surges and ENSO teleconnections) – evaluation of the underlying regional climate drivers helps us understand the reasons behind projected changes in climate variables (rainfall, temperature, humidity and winds).

In addition to the above mentioned aspects of evaluation, we have also analyzed and presented in this chapter the added value of downscaling (reduction in biases as compared to the coarse resolution driving GCM). While the key results from the evaluation of downscaled simulations have been presented in this chapter, more details can be found in the Appendix.

7.2 Data and Methodology

Various observational and reanalysis datasets have been used for evaluating the V3 downscaled model simulations at 8km and 2km resolutions. Even for a single variable we use multiple observational and reanalysis datasets to evaluate the downscaled simulations to account for uncertainties amongst datasets and to make a fair comparison.

We have used both gridded datasets based on in-situ and remotely sensed data and station observations from Singapore to validate the downscaled simulations. We utilize the latest iteration of the PERSIANN CCS CDR precipitation datasets for monthly precipitation analysis, benefiting from its superior spatio-temporal resolution. In the case of diurnal precipitation analysis, we rely on the IMERG dataset due to its exceptional temporal resolution. The gridded and station datasets used for evaluation have been shown in Table 7.1 and briefly described in the subsections below.

Table 7.1: Details of observational and reanalysis data products used for evaluation in this chapter, their climate fields used, and reference. The abbreviation pr refers to precipitation; TAS: surface air temperature; PSL: mean sea level pressure; SST: sea surface temperature; HUSS: specific humidity

NAME	FIELDS (resol./freq.)	REFERENCES
HadCRUT4	TAS (5°x5°, monthly)	Morice et al. 2012
BEST	TAS (1°x1°, monthly)	Rohde and Hausfather, 2020
FROGs	PR (1°x1°, daily)	Roca et al. 2019
IMERG V06	PR (0.1°x0.1°, 30 mins)	Huffman et al., 2019
TRMM 3B42	PR (0.25°x0.25°, 3 hours)	Huffman et al., 2007
PERSIANN_CDR	PR (0.25°x0.25°, sub-daily)	Ashouri et al., 2015
CMORPH_v1	PR (0.25°x0.25°, 3 hours)	Xie et al., 2017
ERA5 reanalysis	SST, TAS, HUSS, PSL, WINDS (0.25°x0.25°, hourly)	Hersbach et al. 2020
MERRA2 reanalysis	SST, TAS, HUSS, PSL, WINDS (0.5° x 0.625°, daily)	Gelaro et al. 2017
JRA55 reanalysis	SST, TAS, HUSS, PSL, WINDS (0.56°x0.56°, sub-daily, monthly)	Kobayashi et al. 2015

7.3 Assessment of large-scale consistency between GCM and RCM

We assess large-scale consistency between the driving model (either ERA5 data or CMIP6 GCMs data for the 8 km downscaling, and 8 km data for the 2 km downscaling) and the downscaler to assess the degree of deviations in the domain mean (SEA domain for 8 km, and WMC domain for 2 km) fields (precipitation, temperature and relative humidity).

Figure 7.1 shows the annual mean time series of precipitation and temperature across Southeast Asia in driving CMIP6 GCM models, and the 8 km downscaled SINGV RCM simulations during historical and SSP5-8.5 scenarios. When compared to the ERA5 during the historical period, the downscaled RCM simulations overestimate the mean precipitation and temperature. The downscaled ACCESS-CM2 simulations captures the interannual variability of the mean precipitation but overestimates the magnitude compared to the driving GCM (ACCESS-CM2). Whereas the time series of mean temperatures in the downscaled simulations closely matches with the driving model (ACCESS-CM2). The EC-EARTH3, downscaled simulations can capture the interannual variations of the mean precipitation and mean temperatures but overestimates the

magnitude of precipitation and temperature, respectively. The MIROC6 model downscaled simulations can capture the interannual variations with an over estimation of the mean precipitation magnitude. Whereas the mean temperature variations and magnitude matches the driving model (MIROC6).

Similar to the MIROC6 and ACCESS-CM2 models, the downscaled simulations of MPI-ESM1-2HR and UKEESM1-0-LL models can capture interannual variability of mean precipitation with a slight overestimation of its magnitude. In contrast, the mean temperature variations and magnitude in downscaled simulation matches with the respective driving models. The NorESM2-MM downscaled simulations also capture interannual variability in the mean precipitation but largely overestimates the magnitude of the mean precipitation by about 30%. The interannual temperature variations of downscaled NorESM2-MM model matches with the driving model with an overestimation of the magnitude.

The downscaled simulations from SINGV are broadly consistent with the driving GCMs. The 8 km downscaled models' climate may have a greater potential for strong convection, which would increase the rate of precipitation compared to the driving GCM models. Most of the downscaled simulations can capture the interannual variability of temperature and precipitation but show a systematic wet bias.
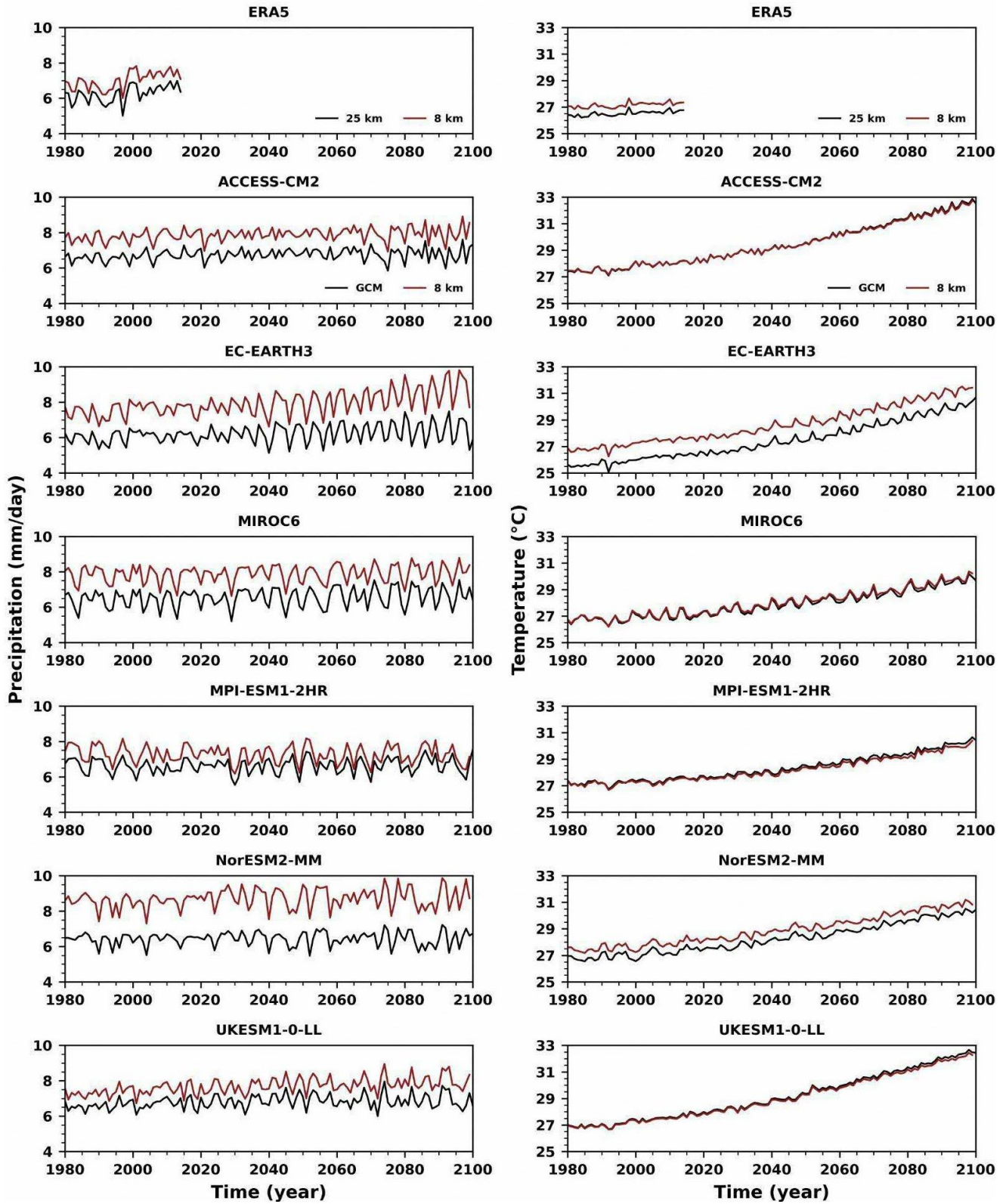
Figure 7.1: Annual mean time series of precipitation (left column) and near-surface air temperature (right column) from driving CMIP6 GCMs (150km; black) and V3 downscaled simulations (8km; red) for historical (1980-2014) and SSP5-8.5 scenario (2015-2099) for SEA region. First row shows the ERA5 reanalysis at its original resolution (25km) and from its corresponding V3 downscaled simulation (8km).

Figure 7.2 shows the annual mean time series of precipitation and temperature across Western Maritime Continent (WMC) from 8 km and 2 km downscaled SINGV simulations during historical and SSP5-8.5 scenarios. During the historical period (1995-2014) using ERA5 data, the interannual variations and magnitude of annual mean precipitation and temperatures from the 8 km simulations closely matches with the 2 km SINGV simulations. The 2 km downscaled time series of temperature and precipitation of ACCESS-CM2, MPI-ESM1-2HR and UKESM1-0-LL models closely aligns (matches the interannual variability and magnitude) with the 8 km downscaled simulations. The 2 km downscaled simulations of NorESM2-MM and EC-EARTH3 models captures the interannual variability of temperature and precipitation similar to that of the 8 km downscaled simulations but overestimates the magnitude of the precipitation slightly higher in the NorESM2-MM.

Overall, the 8 km SINGV downscaled large-scale mean climate of different driving GCM models matches with the 2 km SINGV downscaled fields across the WMC region both in historical and SSP8.5 scenarios. We might notice some spatial (local) changes between the 2 km and 8 km downscaled simulated fields compared to the domain averaged quantities due to better representation of the topographic features in 2 km resolution.
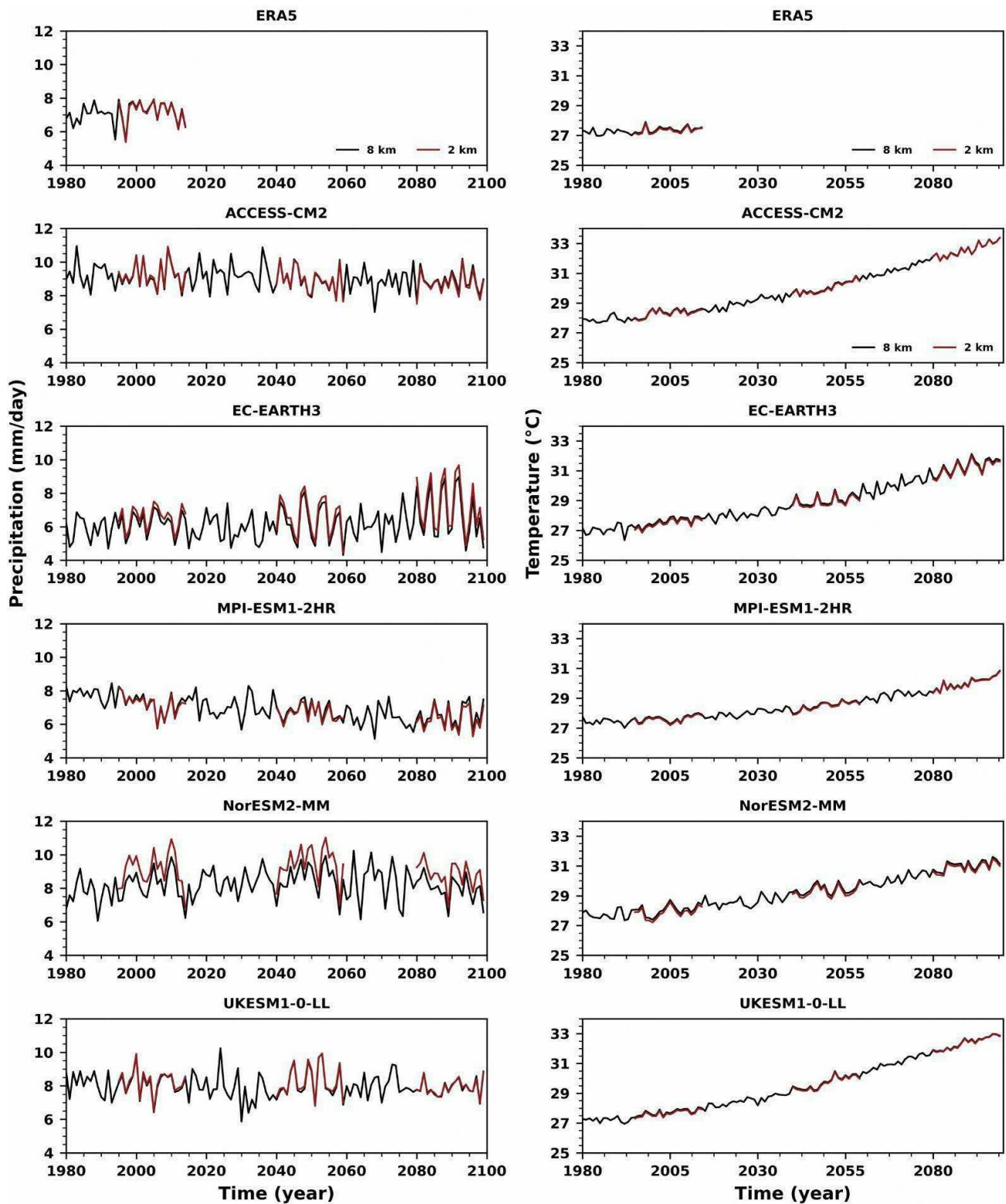
Figure 7.2: Annual mean time series of precipitation (left column) and near-surface air temperature (right column) from V3 downscaled simulations (8 km in blue and 2km in red) for historical (1995-2014) and SSP5-8.5 scenario (2040-2059 and 2080-2099) for WMC region. In the first row, the ERA5 downscaled simulations are shown at 8km and 2km resolutions for precipitation (left) and temperature (right).

7.4 Evaluation of Regional-scale climatology

This section will provide an analysis of mean and extreme rainfall and temperature as well as relative humidity and surface winds simulated by SINGV-RCM.

7.4.1 Mean Rainfall

Figure 7.3a shows that the region generally receives rainfall throughout the domain. Figure 7.3b and d show that relative to PCCSCDR (Sadeghi et al., 2021), SINGV-ERA5 enhances precipitation over areas with significant topography, such as the Sumatran Mountain range, Peninsular Malaysia, Borneo, Sulawesi, New Guinea, and Vietnam. Concurrently, there is a reduction of rainfall over land areas near these regions of high topography, such as east Sumatra and west Borneo. Near the east and west boundaries, there is an enhancement of rainfall over the wetter regions in climatology.
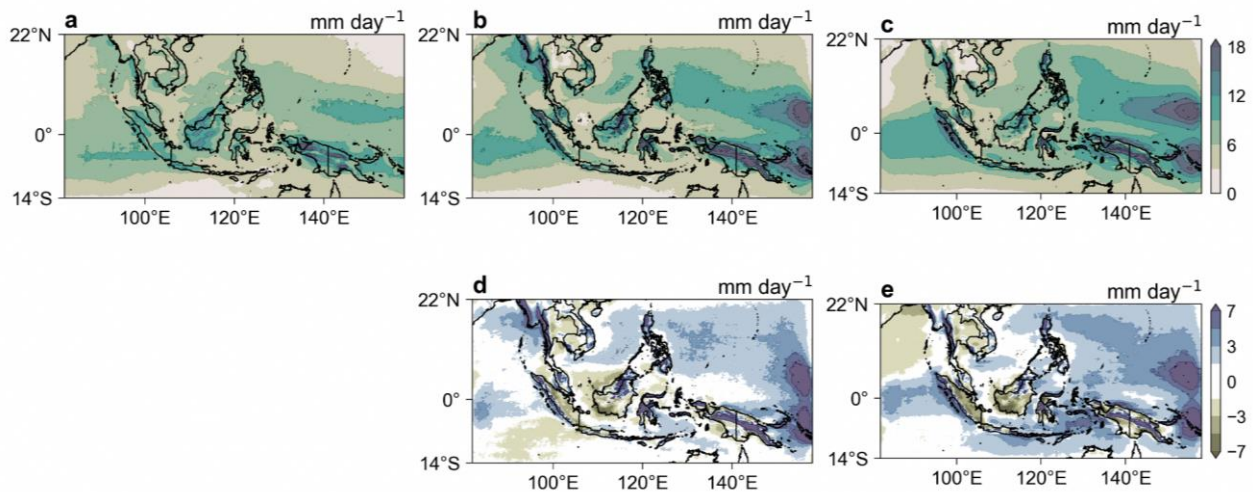

Figure 7.3: Annual mean precipitation (shaded) in (a) PCCSCDR, (b) ERA5 downscaled by SINGV (SINGV-ERA5) (c) Multimodel mean of downscaled GCM simulations with SINGV (SINGV-MMM). (d) shows the bias in SINGV-ERA5 (i.e. b -a), while (e) shows the bias in SINGV-MMM (i.e. c-a).

In DJF, the rainband shifts south of the equator, with Java, Borneo and New Guinea receiving more rainfall and Indochina being relatively dry (Figure 7.4a). Similar to the annual mean, there is an enhancement of precipitation over areas with significant topography and a reduction of precipitation in nearby areas in the downscaled simulation (Fig. 7.4b, d). There is also increased rainfall at the boundaries. SINGV-MMM shares qualitative features with SINGV-ERA5. Relative to SINGV-ERA5, SINGV-MMM simulates less rainfall west of Thailand and east of the Philippines, and increased rainfall over the Java sea (Fig. 7.4d, e). A comparison of land rainfall simulated by downscaled CORDEX models against GPCC by Tangang et al 2020 (see their Fig. 5) also shows a similar moistening in high topography regions, with drying seen parts of the east coast of Peninsular Malaysia and Sumatra and western parts of Borneo.

The rain band moves north of the equator in this JJA season, with a notable rainfall peak falling on the west coast of Indochina and the Philippines (Figure 7.5a). The enhanced rainfall over regions with high topography described in the annual mean can be seen in JJA as well (Figure 7.5b, d), such as over the west coast of Thailand and along Borneo, Sulawesi and New Guinea. In SINGV-MMM (relative to PCCSCDR) (Figure 7.5c, e) there is an enhancement of rainfall east of the Philippines and around Java, and reduced precipitation west of Myanmar. The increased rainfall on the west edge of Indochina is seen in downscaled CORDEX models relative to GPCC (Tangang et al 2020).
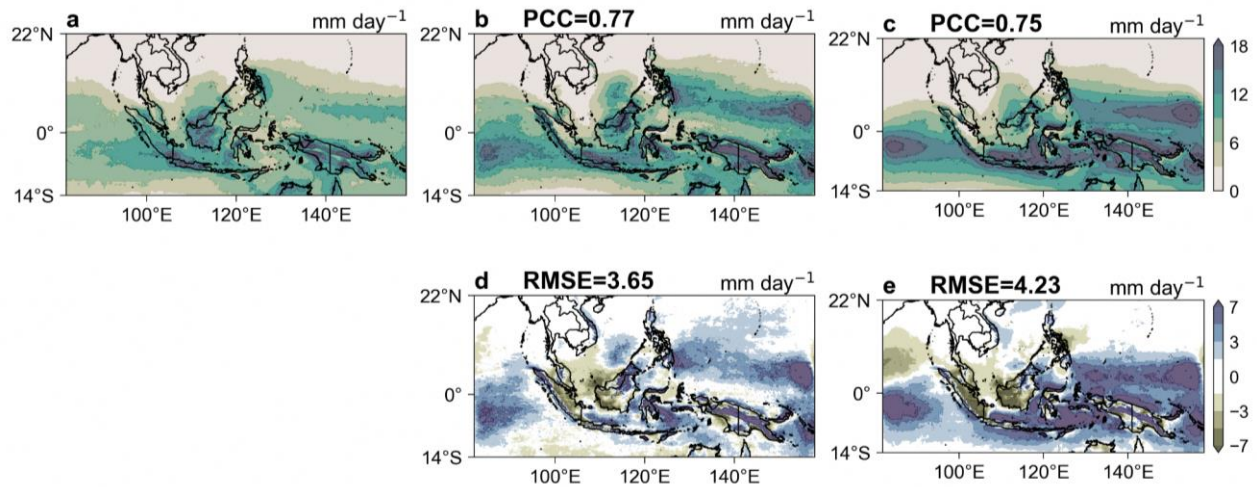
Figure 7.4: DJF mean precipitation (shaded) in (a) PCCSCDR, (b) ERA5 downscaled by SINGV (SINGV-ERA5) (c) Multimodel mean of downscaled GCM simulations with SINGV (SINGV-MMM). (d) shows the bias in SINGV-ERA5 (i.e. b -a), while (e) shows the bias in SINGV-MMM (i.e. c-a).
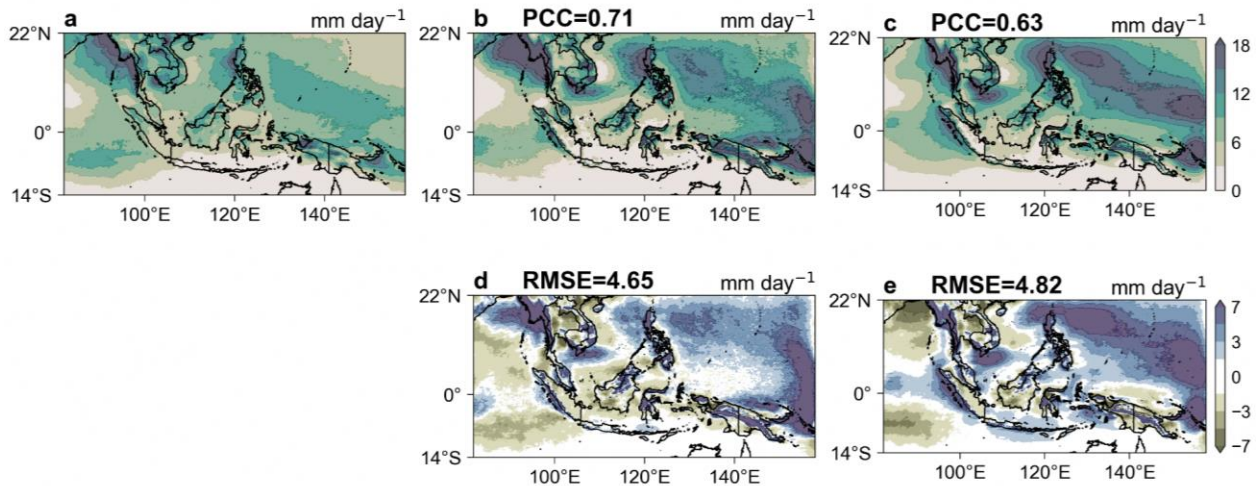

Figure 7.5: JJA mean precipitation (shaded) in (a) PCCSCDR, (b) ERA5 downscaled by SINGV (SINGV-ERA5) (c) Multimodel mean of downscaled GCM simulations with SINGV (SINGV-MMM). (d) shows the bias in SINGV-ERA5 (i.e. b -a), while (e) shows the bias in SINGV-MMM (i.e. c-a).

Annual cycle:

The annual cycle of rainfall over the Southeast Asia and Western Maritime Continent regions varies on monthly scale due to different large-scale drivers (ENSO, IOD, MJO), local drivers (sumatra squalls, northeast monsoon surges, Borneo vortex) and seasonal transition of the ITCZ. Here, we use the observational data from Precipitation Estimation from Remotely Sensed Information using Artificial Neural Networks (PERISANN), and model data from 2 km and 8 km downscaled simulations using ERA5 data. Figure 7.6 shows the area averaged precipitation annual cycle over the Southeast Asia (8 km; blue line) and Western Maritime Continent (8 km & 2 km; orange line) using SINGV RCM downscaled simulations and PERISANN (black line) over land & ocean, land only and ocean only regions (shading denotes the spread between models).

Over the SEA (Land & Ocean), and SEA (Ocean) domains, the 8 km simulation is able to capture the observed (PERISANN) annual cycle with peak precipitation during July. The SEA land precipitation annual cycle in 8 km downscaled simulation shows peak precipitation in July which is not observed in PERSIANN (peak during May). Overall, the land only precipitation annual cycle over the SEA is not captured well in the 8 km downscaled SINGV simulations.
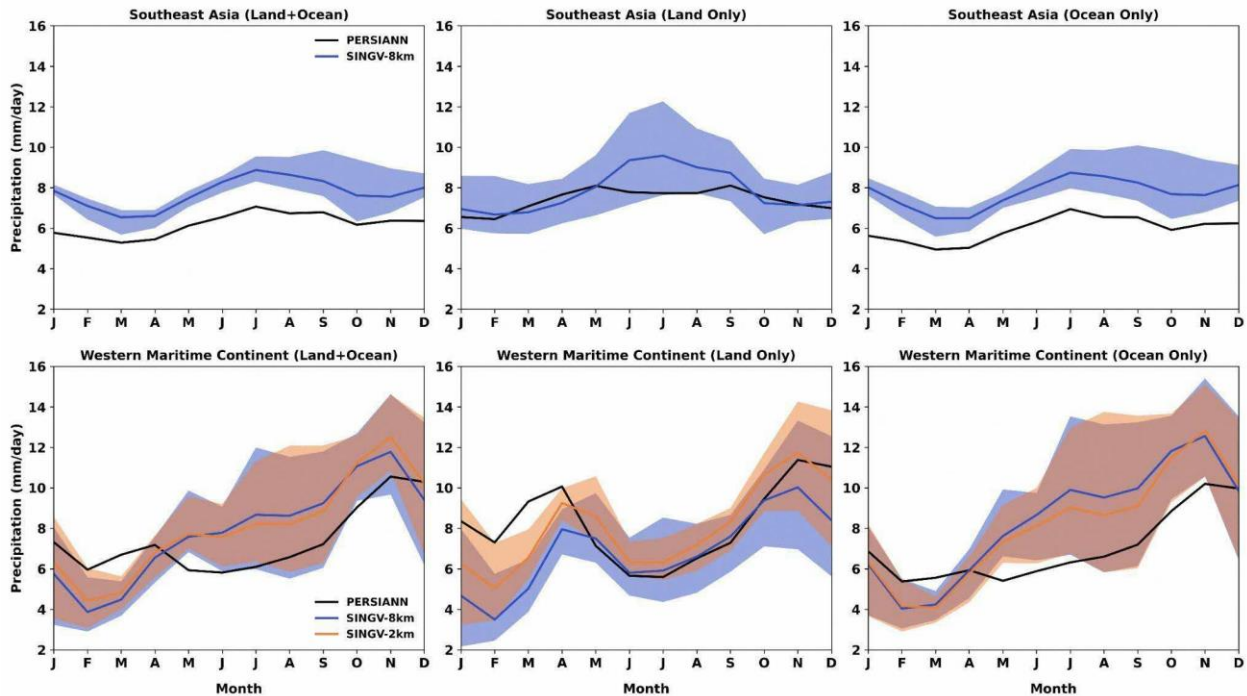

Figure 7.6: Annual cycle of precipitation (mm/day) from downscaled simulations for the historical period (1995-2014) for Southeast Asia (8km) and WMC (8km and 2km) for land + ocean, land only and ocean only. For observations, multiple datasets were used and are shown in black. The climatological period for observations varies as in Table 1.

In the WMC (land & Ocean) domain, the precipitation annual cycle in observations varied with both the 2 km and 8 km downscaled simulations during May and June. The downscaled simulations overestimates the observed precipitation magnitude in the months May to November and underestimates it in the months of January to April. In addition, there is a large intermodal difference during the southwest monsoon season i.e. July to September.

In the WMC (land only) domain, the annual cycle of precipitation is captured reasonably well by 2 km and 8 km downscaled simulations but underestimates the magnitude (greatly by 8 km simulation) compared to observations during January to April. The precipitation is overestimated in 2 km downscaled simulations from May to November compared to observations and 8 km simulations.

In WMC (ocean only), the observed annual precipitation cycle is not captured well by the 2 km and 8 km downscaled simulations during April and May. The precipitation from April to November is overestimated in both the 2 km and 8 km downscaled simulations. Also, there is a large intermodal difference during the southwest monsoon season (JJAS).

Overall, the mean precipitation annual cycle over the SEA region (Land & Ocean, Ocean) from 8 km and 2 km downscaled simulations is comparable to the observed annual cycle (PERISANN) with a difference in magnitude. The Land-only precipitation annual cycle over SEA is not captured well by the downscaled simulations. The WMC region's annual precipitation cycle using the 8 km and 2 km downscaled simulations (large intermodal spread during the southwest monsoon season) vary compared to the observed annual

cycle over Land & Ocean and Ocean only domains. The WMC region's observed land only precipitation annual cycle is captured by 2 km and 8 km downscaled simulations with a difference in magnitude.

Diurnal Cycle

The diurnal cycle of rainfall is an important component of rainfall variability in the Maritime Continent. We use hourly data from observations (IMERG) and model data from 8 km and 2 km simulations for evaluating the diurnal cycle of rainfall. Figure 7.7 shows the area averaged diurnal precipitation cycle over the 2 km WMC dynamical downscaling domain, for two seasons JJAS(a) and NDJF(b). We see from Figure 7.7a that SINGV-RCM 8 km and 2 km with explicit representation of convection is able to capture the diurnal timing of precipitation over land grid points, and the timing matches well with observation (IMERG) but the magnitude does not, and this is worse in the 2km model, for JJAS season.
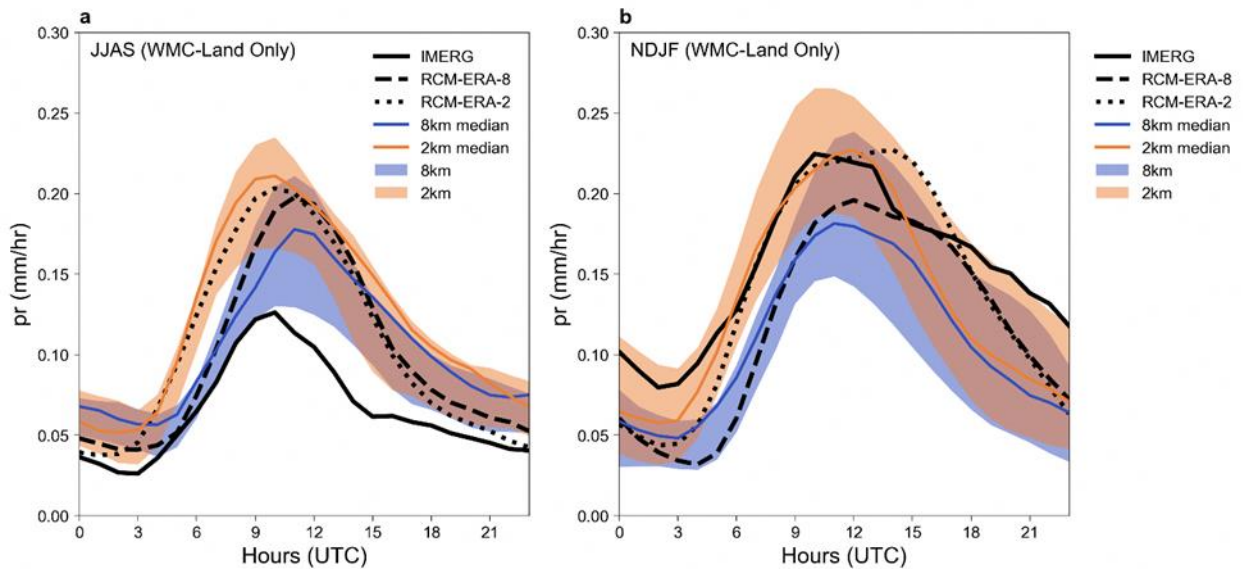

Figure 7.7: Diurnal cycle of Precipitation area averaged over WMC domain for JJAS and NDJF. a) Ensemble median and spread for SINGV-2km and SINGV-8km compared to IMERG-obs (JJAS), b) Ensemble median and spread for SINGV-2km and SINGV-8km compared to IMERG-obs (NDJF). Units in mm/hr. Note that Singapore is 8 hours ahead of UTC. The precipitation peak is around the late afternoon of Singapore local time.

Blue line for 8 km model runs and Orange line for 2 km (shades denote the spread among the models), however the downscaling to 8 km and 2 km improves the diurnal timing, we do see the added value from 8 km to 2 km, though we see improvement in the timing compared to GCM (which is not shown here), we do see the intensity is more in 8 km compared to IMERG and even more intense when we drive 2 km by 8 km output for JJAS.

The results are quite similar for NDJF as well (Figure 7.7b). High resolution runs of 2 km have a better diurnal peak timing (improvement) compared to 8 km run, while the intensity (Land grid points only) is over predicted by SINGV-RCM for JJAS season (Figure 7.7 a). Whereas the SINGV-RCM at 8 km resolution is under predicted for NDJF season compared to observation (Figure 7.7 b), while the 2km resolution corrects it (improvement). Figure 7.8 shows the spatial variation in the timing of the diurnal rainfall peak over the WMC domain compared to GPM-IMERG data at each grid point.
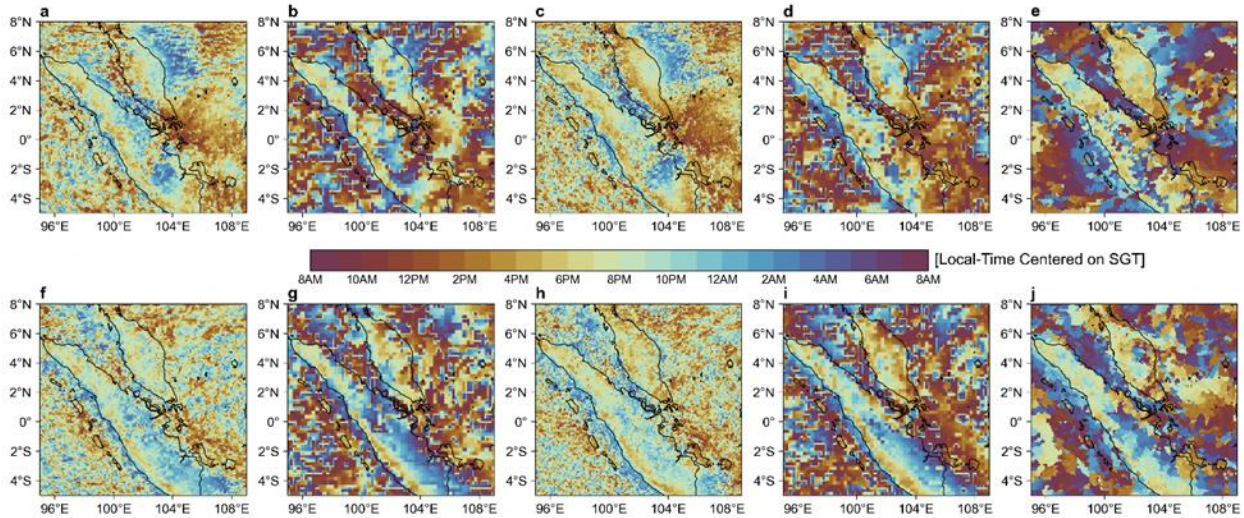
Figure 7.8: Spatial map of Peak Diurnal timing of Precipitation for JJAS and NDJF. a) Ensemble mean of SINGV-8km (JJAS), b) SINGV-8km-ERA (JJAS) c) Ensemble mean of SINGV-2km (JJAS), d) SINGV-2km-ERA (JJAS), e) IMERG-obs (JJAS). f) Ensemble mean of SINGV-8km (NDJF), g) SINGV-8km-ERA (JJAS), h) Ensemble mean of SINGV-2km (NDJF), i) SINGV-2km-ERA (JJAS), j) IMERG-obs (NDJF). Units in hour (SGT).

The spatial variation in timing of the peak rainfall for this region: earlier times over land seem largely tied to the higher orography while over much of the lower orography the peak occurs overnight/early morning (Based on Singapore local time), hence the second peak in Fig. 7.7b. There is also a later peak along the Sumatran coast and an earlier peak over and beyond the islands off the coast. The models do seem to capture this spatial variation.

7.4.2 Rainfall Extremes

Here we used the annual maximum 1-day precipitation (RX1day) to evaluate RCM's fidelity simulating the rainfall extremes. Based on the evaluation (Figure 7.9), it is observed that both SINGV-ERA5 and SINGV-MMM models tend to overestimate RX1day across the Southeast Asia (SEA) domain. This overestimation is consistent with the overestimation of the annual mean rainfall in these models.
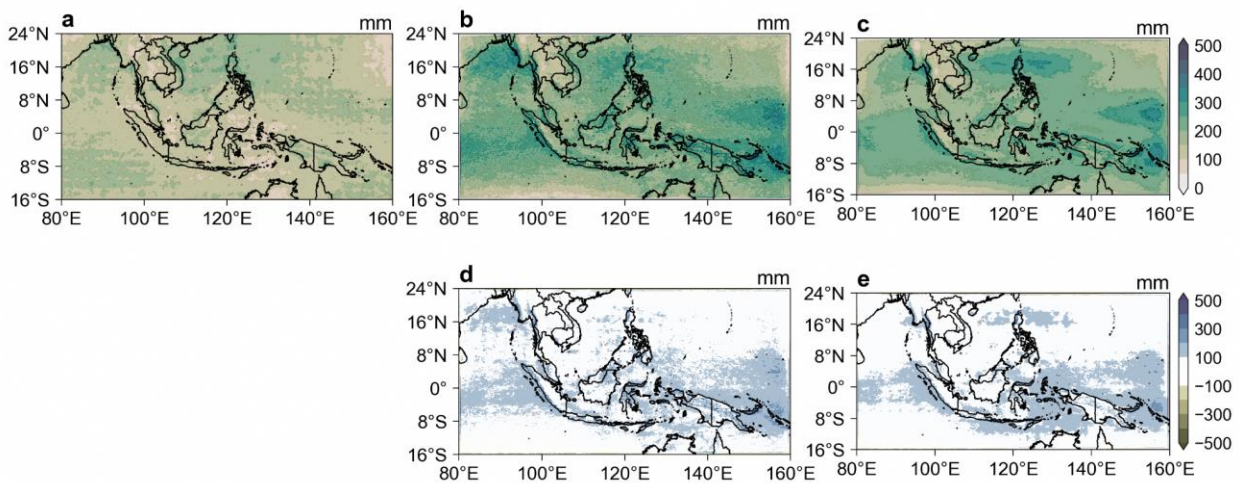

Figure 7.9: Annual RX1day in (a) PCCSCDR, (b) ERA5 downscaled by SINGV (SINGV-ERA5) (c) Multimodel mean of downscaled GCM simulations with SINGV (SINGV-MMM). (d) shows the bias in SINGV-ERA5 (i.e. b -a), while (e) shows the bias in SINGV-MMM (i.e. c-a).

It suggests that there might be a common bias in the representation of precipitation processes in these models, leading to an overestimation of both mean rainfall and extreme precipitation events. Specifically, the overestimation of RX1day is more prominent in the equatorial SEA region, while the biases in the extratropical region are relatively smaller. This spatial pattern of biases suggests that there may be certain factors or processes specific to the equatorial region that contribute to the overestimation of extreme rainfall events. These results can help identify areas where improvements are needed in the representation of precipitation processes in the RCMs, particularly in capturing the characteristics of extreme rainfall events in the equatorial SEA region.

7.4.3 Mean Temperature

Figure 7.10 shows the annual cycle of mean temperature over the SEA and WMC regions from HadCRUT observations (black line), 8 km (blue line), and 2 km (orange line) downscaled simulations for the historical period. The annual cycle of temperature in the SEA and WMC regions vary across months over land & ocean, land only, and ocean-only domains.

Over the SEA (Land & Ocean) domain, the annual cycle has a bimodal distribution with peak temperatures in May and October. The 8 km downscaled simulations are able to capture the observed annual cycle with a slight underestimation of temperatures during Jan-Apr, and Sep-Dec.

Over the SEA (land only) domain, the observed annual cycle has bimodal distribution with peak temperatures during May and October. The 8 km downscaled simulations can capture one of the peaks during May but cannot capture the other one. The temperatures are significantly underestimated by about 2oC over SEA land in the downscaled simulations. The cold biases are observed in 8km-downscaled simulations similar to the cold biases in the GCMs over the Indochina region (section 5.3.1 Figure 5.2). Over SEA (ocean only), the observed annual cycle of temperature is captured well by the 8 km downscaled simulations.
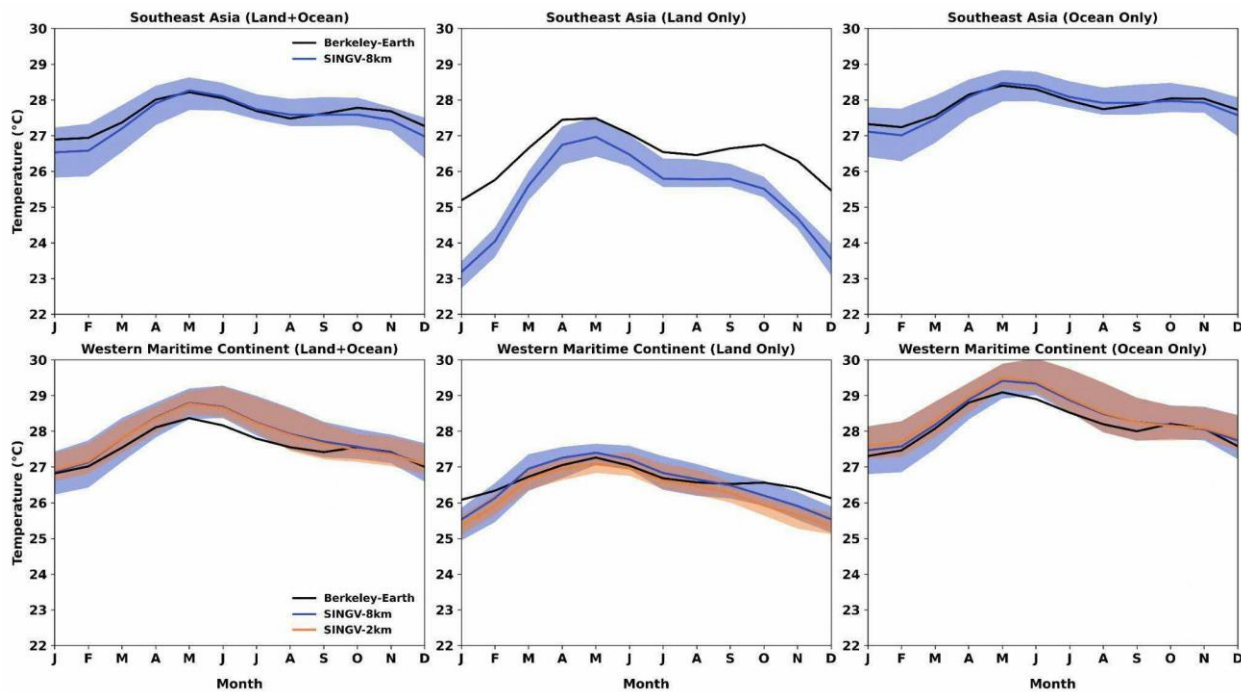

Figure 7.10: Annual cycle of temperature (deg C) from downscaled simulations for the historical period (1995-2014) for Southeast Asia (8km) and WMC (2km) for land+ocean, land only, and ocean only. For observations, HadCRUT is used for 1995-2014.

The observed mean annual cycle of temperature over the WMC region (Land & Ocean) has bimodal distribution with peak temperatures during May and October. The 8 km and 2 km downscaled simulations are able to capture the annual cycle but slightly overestimate the magnitude.

Over the WMC (Land only) domain, both the 8 km and 2 km simulations are able to capture the observed annual cycle with a slight underestimation of the magnitude. The WMC (ocean only) observed temperatures show bimodal distribution with peaks during May and October. Both the 8 km and 2 km downscaled simulations are able to capture the annual cycle but slightly overestimate the magnitude.

The historical annual temperature cycle over the SEA and WMC regions is captured reasonably well by 2 km and 8 km downscaled simulations. The 8 km downscaled simulations significantly

underestimate the temperatures over the SEA (Land only) domain.

7.4.4 Temperature Extremes

The extreme temperatures are measured using the annual (or monthly) maximum of daily maximum surface temperatures (TXx). Figure 7.11 shows the TXx over the SEA land regions in ERA5 land (a), ERA5 downscaled SINGV (b), and Multimodel mean of the downscaled GCM simulations (c). As seen in the Fig. 7.11(d, e), both the ERA5 downscaled simulations and multimodel mean of downscaled simulations overestimate the TXx temperatures across most of the SEA nations (underestimate over New Guinea) with a higher magnitude of differences in GCM downscaled simulations (7.11d). Overall, the SINGV downscaled model simulations can capture the spatial pattern of historical extreme temperatures over the SEA nations with a difference in the magnitude of temperatures.
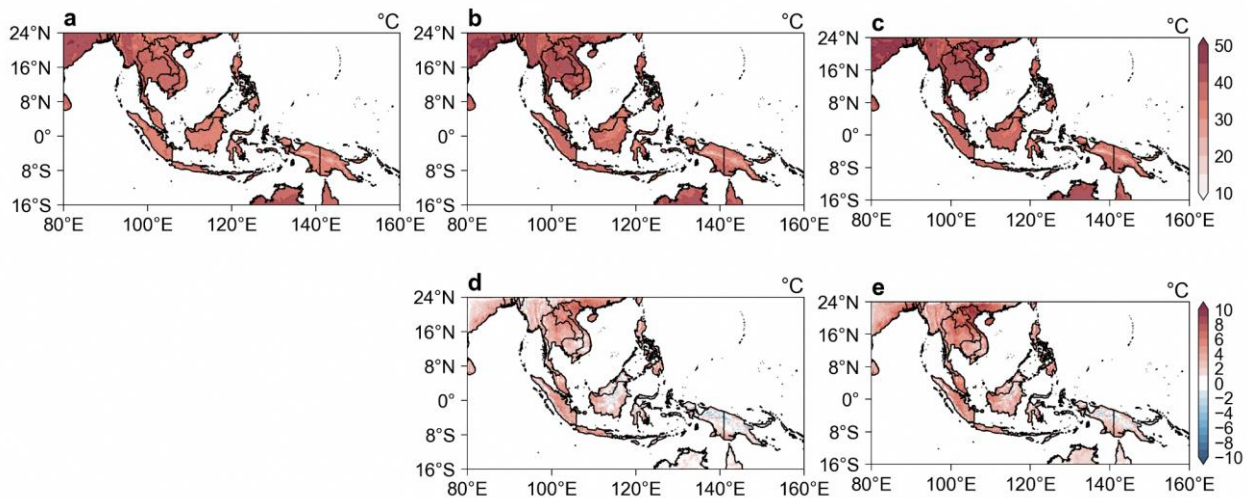

Figure 7.11: Annual TXx in (a) ERA5 Land (b) ERA5 downscaled by SINGV (SINGV-ERA5) (c) Multimodel mean of downscaled GCM simulations with SINGV (SINGV-MMM). (d) shows the bias in SINGV-ERA5 (i.e. b -a), while (e) shows the bias in SINGV-MMM (i.e. c-a).

7.4.5 Relative Humidity

Humidity is a measure of the water vapor concentration in air. Relative humidity is expressed as a percentage, which measures the amount of water vapor in the air relative to the maximum amount the air can hold at a given temperature and pressure. Figure 7.12 shows the annual cycle of Relative humidity (RH) across the SEA and WMC regions from observations

(ERA5), and downscaled simulations (2 km and 8 km) during the historical period.

Over the SEA (Land & ocean) domain, the 8 km downscaled simulations of different driving GCM models can capture the observed annual variations of RH (maximum values during the southwest monsoon season) but underestimate RH magnitude. The SEA (land only), the 8 km downscaled simulations can capture the observed

annual cycle but significantly underestimate RH magnitude by about 4% compared to ERA5. The SEA (ocean only), 8 km downscaled annual cycle

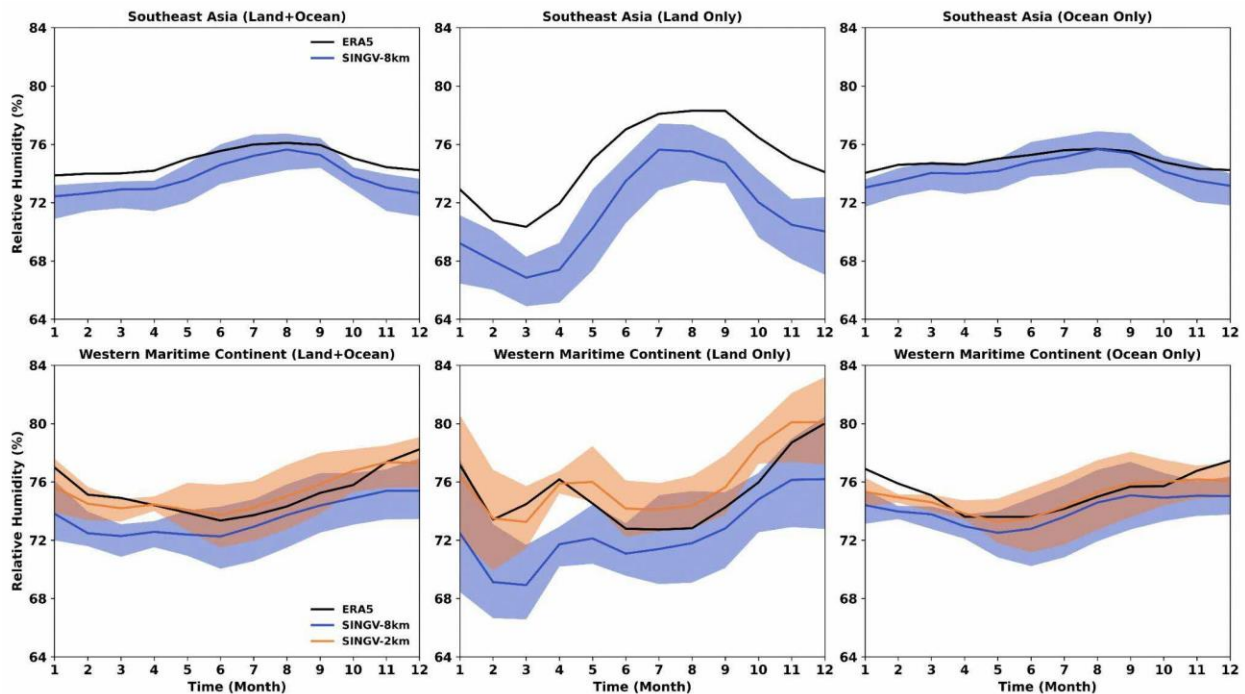matches the observed annual cycle with an underestimation of the magnitude.

Figure 7.12: Annual cycle of relative humidity from downscaled simulations for the historical period (1995-2014) for Southeast Asia (8km) and WMC (8km + 2km) for land+ocean, land only, and ocean only. For observations, ERA5 data is used for 1995-2014.

Over the WMC (Land & Ocean), the 2 km downscaled model simulations match better with the RH in ERA5 compared to the 8 km downscaled simulations. For the historical RH annual cycle, the 2 km downscaled simulations also capture it but slightly underestimate during January to April and overestimate during April to November.

The WMC (Land only) 8 km and 2 km downscaled simulations can capture the historical RH annual cycle. The 8 km downscaled simulations significantly underestimate the magnitude and 2 km simulations slightly overestimate. The WMC (Ocean only) downscaled simulations (2 km and 8 km) can capture the annual cycle but slightly underestimate compared to the ERA5. Overall, the annual cycle of RH is captured in 2 km and 8 km downscaled SINGV simulations but underestimate the RH magnitude (largely by 8 km downscaled simulations).

7.4.6 Winds

Ali et al (2022) evaluated five CORDEX-SEA simulations of downscaled wind speed and concluded that all models were able to reproduce the spatial pattern of wind speed well, but only described three models as being able to correctly reproduce the wind direction. In a comparison of a 14-member ensemble simulation, Tangang et al (2020) noted that the patterns of bias in the RCM were generally similar to those of the parent GCM, although the RCM could make modification in some cases, such as strong southerlies in the eastern Indian Ocean and west of Sumatra. Their results also indicate a general strengthening of the bias in the downscaled simulations of the westerlies over Indochina in JJA. As for DJF, the largest biases in the multi-model mean were easterly over Indochina and westerly over much of Java.

In JJA (Figure 7.13), the southwesterly flow is strongest over the Indian ocean. Downscaling in SINGV-ERA5 enhances the westerly flow from the Andaman Sea to the Philippines relative to ERA5.

This strengthening of the monsoonal flow is enhanced for SINGV-MMM, similar to the multimodel mean JJA results of Tangang et al (2020) and the westerly bias of the 6 CMIP6 models over part of Indochina (Figure 7A.1). In contrast, the southwesterly flow for SINGV-NorESM2-MM is displaced southwards towards Sumatra, while that of MIROC6 is weaker than ERA5 (not shown). Martin et al. (2021) have noted a similar westerly bias over Indochina in the GC2 configuration of the Unified Model (UM), on which SINGV-RCM is based. Their result, combined with the occurrence of this bias even when forced with ERA5 at the boundaries (panel d), suggests that the bias is inherent in the UM. In addition, because SINGV-RCM is run with explicit convection, the development of this bias is not solely linked to the convection scheme employed by the UM.
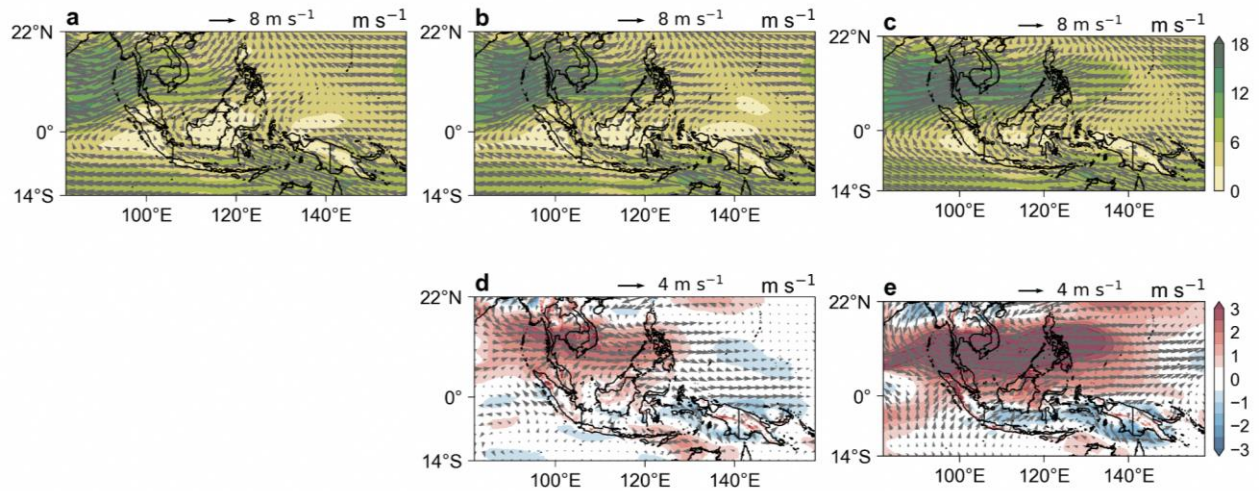

Figure 7.13: Mean JJA 850 hPa winds (quivers) and wind speed (shaded) in (a) ERA5, (b) ERA5 downscaled by SINGV (SINGV-ERA5) (c) Multimodel mean of downscaled GCM simulations with SINGV (SINGV-MMM). (d) shows the bias in SINGV-ERA5 (i.e. b -a), while (e) shows the bias in SINGV-MMM (i.e. c-a).

In DJF (Figure 7.14), the northeasterly flow reaches a peak in wind speed off the south coast of Vietnam, and turns southeasterly after crossing the equator. Downscaling in SINGV-ERA5 creates a cyclonic anomaly centered on south Vietnam, as well as enhancing the westerlies off the east coast of Borneo towards the Celebes Sea. Except for SINGV-ACCESS-CM2 (not shown), this feature is not particularly apparent in the downscaled GCMs and SINGV-MMM. Instead, the flow in SINGV-MMM is more northerly over the South China Sea along the east coast of the Malay Peninsula and towards Singapore. The downscaled simulations show small or northeasterly bias over Indochina, and a spread of wind bias over Java (not shown), which differ from the CMIP5 CORDEX-SEA downscaling findings of Tangang et al (2020) described above. A northeasterly bias in parts of Indochina can be seen in the multimodel mean of the 6 GCMs used for downscaling (Figure 7A.2).
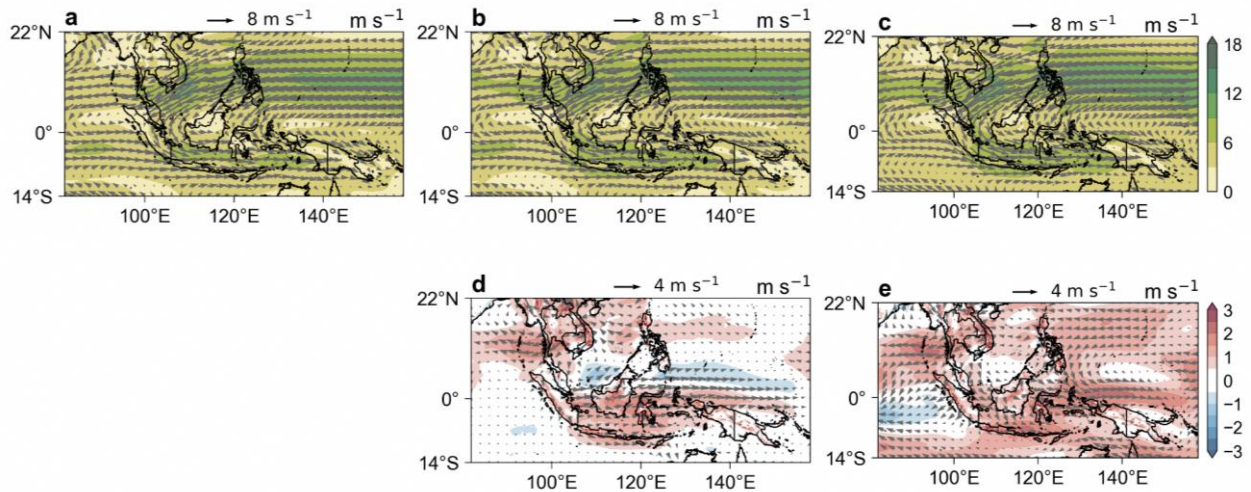
Figure 7.14: Mean DJF 850 hPa winds (quivers) and wind speed (shaded) in (a) ERA5, (b) ERA5 downscaled by SINGV (SINGV-ERA5) (c) Multimodel mean of downscaled GCM simulations with SINGV (SINGV-MMM). (d) shows the bias in SINGV-ERA5 (i.e. b -a), while (e) shows the bias in SINGV-MMM (i.e. c-a).

7.5 Evaluation of regional climate drivers

The biases in the simulation of climate variables are associated with simulation biases of the key climate drivers. In this subchapter we show the biases in the simulation of three important climate drivers - northeast monsoon surges, ENSO teleconnections, and weather regimes.

7.5.1 Monsoon

Monsoons have a key role in shaping the weather and climate of the MC domain. The MC domain is affected by the boreal summer (JJA) monsoon as well as the boreal winter (DJF) monsoon. Seasonal migration of ITCZ leads to climatological rainfall peaks during the monsoon season in Northern and Southern hemispheres.

Figure 7.15 (top left panel) shows the observed (based on PERSIANN-CCS data) migration of monsoon rainfall for the 1995-2014 period with northern hemisphere (NH) peaks during JJAS and southern hemisphere (SH) peaks in DJFM. Note the more persistent wet all year around in the equatorial region. Also, there is north-south asymmetry across the equator, with the NH monsoon extends further north compared to the SH monsoon extension southward.
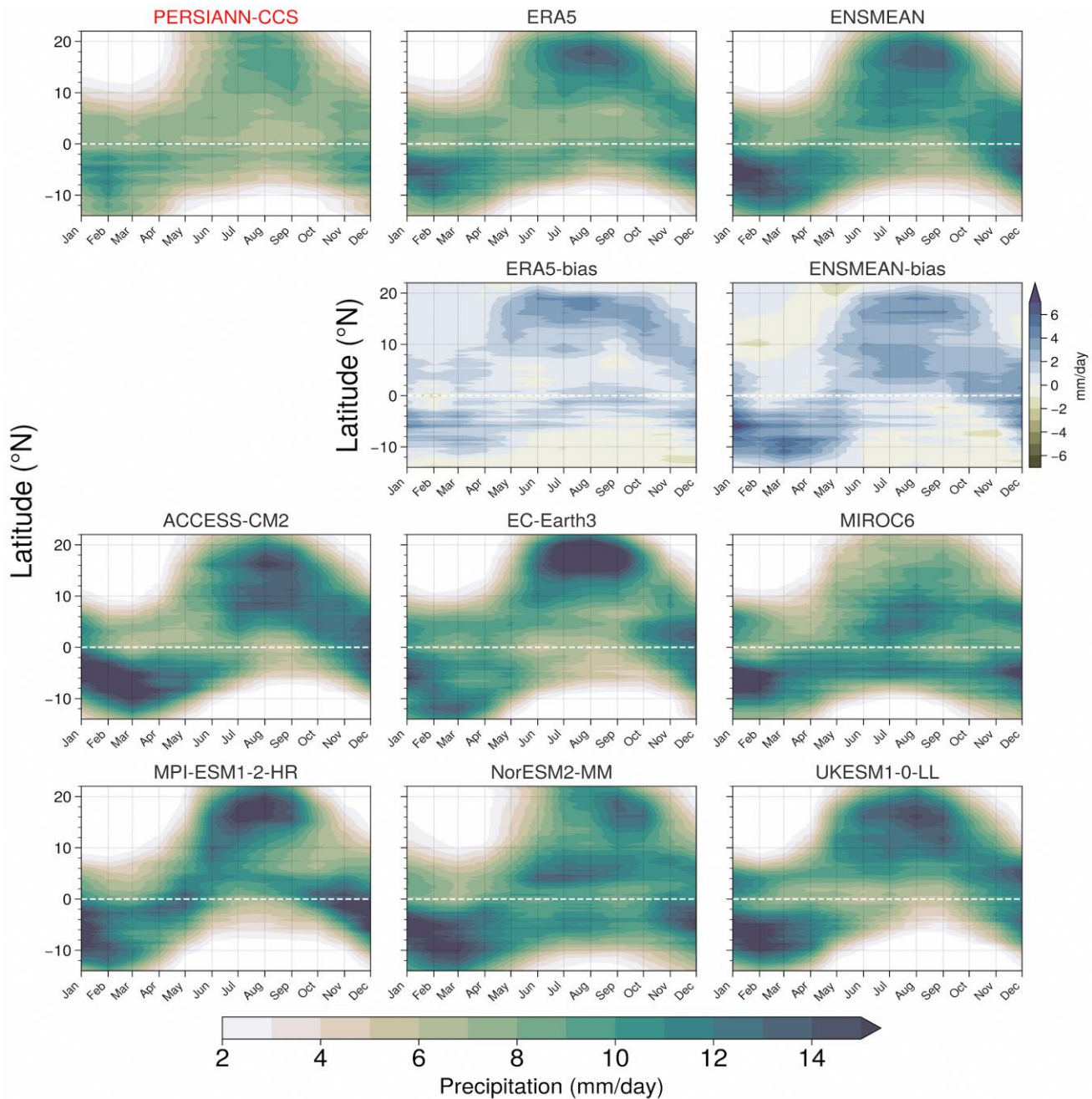
Figure 7.15: The time-latitudinal progression of zonally-averaged (80-160E) climatological monthly precipitation (i.e. passage of the ITCZ-monsoon rain belt) for the period 1995-2014 in high-resolution satellite observations (PERSIANN-CCS; regridded to 8-km) and in SINGV-RCM 8-km downscaled simulations of ERA5 and the six sub-selected GCMs (ACCESS-CM2, EC-Earth3, MIROC6, MPI-ESM1-2-HR, NorESM2-MM and UKESM1-0-LL). The multi-model ensemble mean (ENSMEAN) of the six downscaled GCMs is shown in the top right panel. Biases in the SINGV-ERA5 and ENSMEAN progression of the ITCZ rain belt are shown in the second row.

Compared to the observation reference, SINGV-ERA5 (Figure 7.15 middle panel in the 1st and 2nd rows) shows that overestimated rainfall in the NH (~15N) during the summer monsoon season (JJAS) and also overestimated rainfall in the SH (~8S) during the winter monsoon season. Multimodel mean of SINGV-RCM (SINGV-MMM) shows similar biases of overestimated monsoon rainfall as the SINGV-ERA5. Within the equatorial region, SINGV-RCMs tend to show a larger bias

compared to the SINGV-ERA5. Six RCMs overall show reasonably realistic monsoon rainfall across the year, but we do observe model diversity (Figure 7.15 lower panels), e.g., EC-Earth3 appears to have a much stronger summer monsoon rainfall while MIROC6 has weaker summer rainfall compared to other models.

Similar to significant positive bias of precipitation in a latitude band of 10-20N observed in GCM-MMM (Fig.5.14), the downscaled simulations of SINGV-RCM (8km) also show significant positive precipitation bias around the similar latitudinal band (Fig. 7.15)

7.5.2 Northeast Monsoon surge

Figure 7.16 shows the spatial pattern of mean rainfall and 850hPa winds composited over surge days (as defined in Chapter 7) for the period 1995-2014 from observations/reanalysis and downscaled 8 km simulations. Also shown are the corresponding biases. The reference (Fig. 7.16a) shows northeasterly winds over the South China Sea characteristic of surge days. After crossing the equator, the winds turn northwesterly. In the process, these winds bring heavy rainfall to the Maritime Continent, especially over the Philippines and Borneo.

Figures 7.16b and d show that SINGV-ERA5 is able to capture the wind features, with increased precipitation over the Java Sea, Sulawesi, and New Guinea, as well as the Indian ocean, and an eastward shift of the precipitation peak over Borneo. There are anomalous winds directed eastward from Borneo, as well as anticyclonic winds around Myanmar.

In SINGV-MMM (Figures. 7.16c and e; computed from the multi-model mean of the 6 downscaled 8 km simulations), there is a southward shift of precipitation, with strong precipitation over the Indian ocean and east of Borneo. Similar to GCM bias (Fig. 5.24c) we observe dry bias over Philippines and wet bias over Sulawesi in the downscaled SINGV-MMM (Fig.7.16e).

The surge frequency of the reference (not shown) is 19% which matches that of SINGV-ERA5 (19%). Other than MIROC6 (12%), the downscaled models have surge frequencies ranging from 15% in ACCESS-CM2 to 20% in UKESM1-0-LL, with a multi-model mean of 17%. This is consistent with the driving GCMs, where GCMs generally had lower surge frequencies as compared to reanalysis.
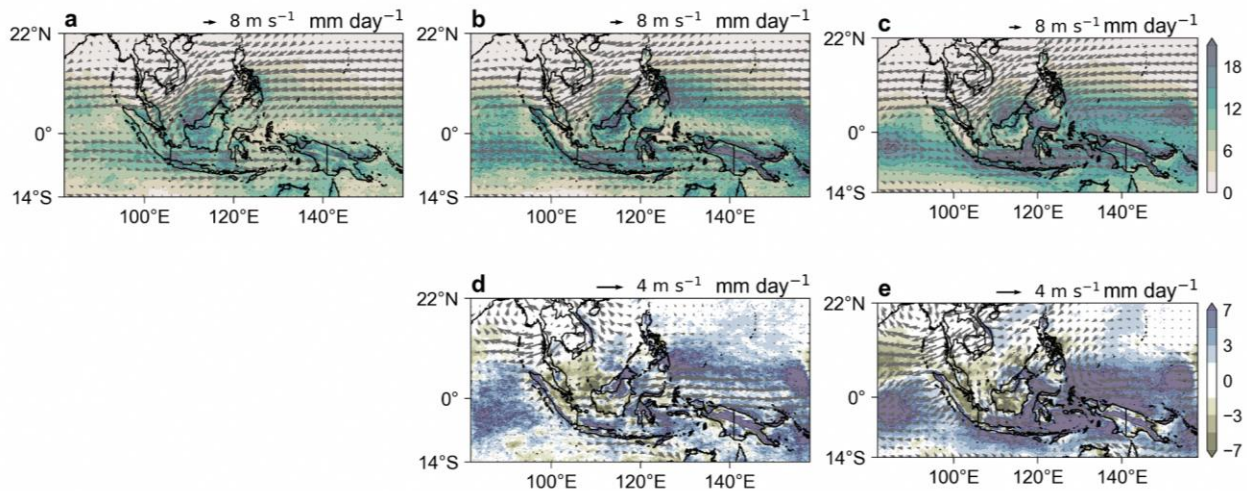

Figure 7.16: Mean 850 hPa winds (quivers) and rainfall (shaded) composited over surge-days in (a) REF (surge days and surge winds derived with ERA5 winds and sea level pressure, and using PERSIANN-CCS-CDR rainfall), (b) ERA5 downscaled by SINGV (SINGV-ERA5) (c) Multimodel mean of downscaled GCM simulations with SINGV (SINGV-MMM). (d) shows the bias in SINGV-ERA5 (i.e. b -a), while (e) shows the bias in SINGV-MMM (i.e. c-a). The reference and model datasets have different resolutions, so we use the lower of the two resolutions. For surge days and wind composites, this is 25km following the resolution of ERA5. For rainfall, values are computed at 8km resolution (following that of SINGV-RCM).

7.5.3 ENSO Teleconnections

Evaluation of the simulation of ENSO-rainfall teleconnection is proposed as one of the metrics to test the fidelity of RCMs (Torres-Alavez et al. 2021). The main goals of this evaluation are to assess: 1. whether RCMs and driving GCMs reproduce the observed large scale ENSO teleconnection patterns; 2. whether the ENSO signal propagates correctly from the driving GCMs to the RCMs; 3. whether the higher resolution of RCMs can improve the ENSO teleconnection in certain parts of the domain.

Here we analyze ENSO teleconnection over the Maritime Continent in the historical period (1995-2014) in all seasons. The observation reference is calculated using 8 km resolution PERSIANN-CCS-CDR monthly rainfall and HadISST Nino3.4 index. For the JJA season, the observed teleconnection shows negative rainfall variability induced by El Nino near the central/western MC while positive rainfall variability near the western Pacific and Northern MC (Figure 7.17a). We calculate ENSO-rainfall teleconnection in the RCM using RCM rainfall and Nino3.4 index from the corresponding driving GCM. The comparison shows that RCMs are able to reproduce consistent spatial patterns as the corresponding driving GCMs (Figure 7.17).

We further calculate two measures to compare teleconnection in RCMs and GCMs to the observation: 1. RMSE between spatial patterns of the teleconnection, 2. Correlation coefficient (corrcoeff) between spatial patterns. The results show that RCMs have similar RMSE as their corresponding driving GCMs (Figure 7.18).

RCMs have slightly lower spatial agreement with the observation compared to the driving GCMs (Figure 7.19). Across the season, RCMs have lower RMSE but similar corrcoeff to GCMs in MJJ and higher RMSE, lower corrcoeff for most of the rest of the year. The corrcoeff in RCMs is generally lower in April-July than in the other months. Note that it is difficult to identify the origins of detailed differences between GCMs and RCMs given multiple possible causes, such as spatial resolution, different physics schemes, etc.
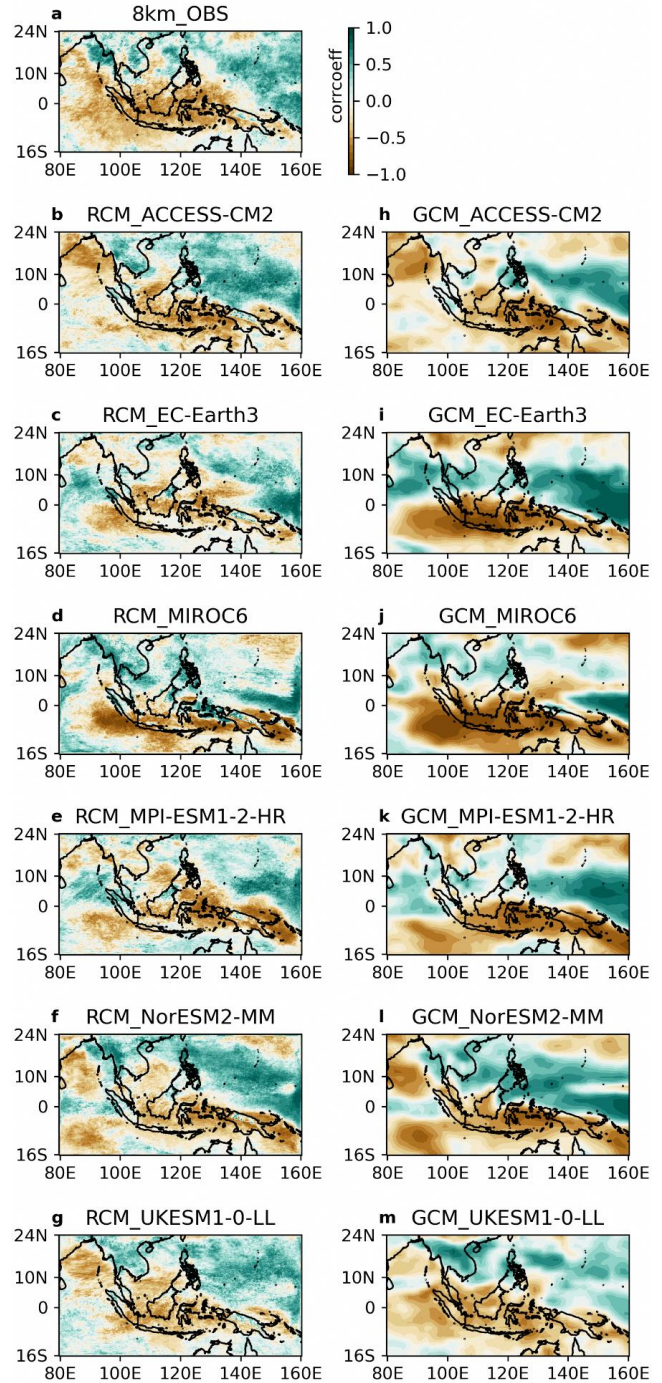

Figure 7.17: JJA ENSO-rainfall teleconnection over the Maritime Continent using correlation [corr (N34, pr)]. a. 8km resolution observation using TS_HadISST and PR_PCCSCDR. b-g. 8km resolution RCMs. h-m. GCMs remapped to 8km to facilitate the visual inspection.
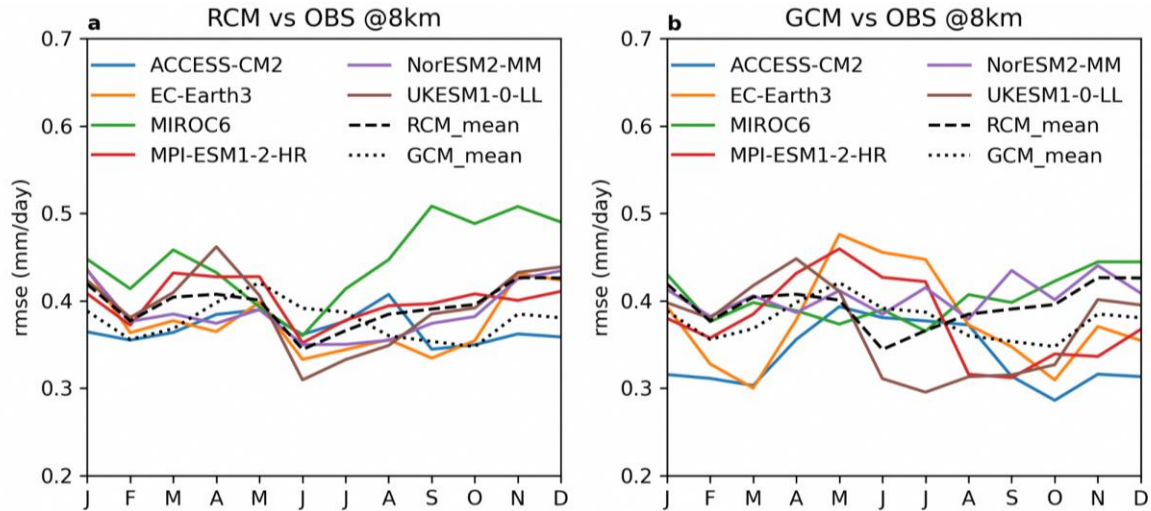
Figure 7.18: RMSE between the 8km observation and RCMs (a) or GCMs (b) over the MC region as to the ENSO teleconnection in the JJA season of the historical period (1995-2014).
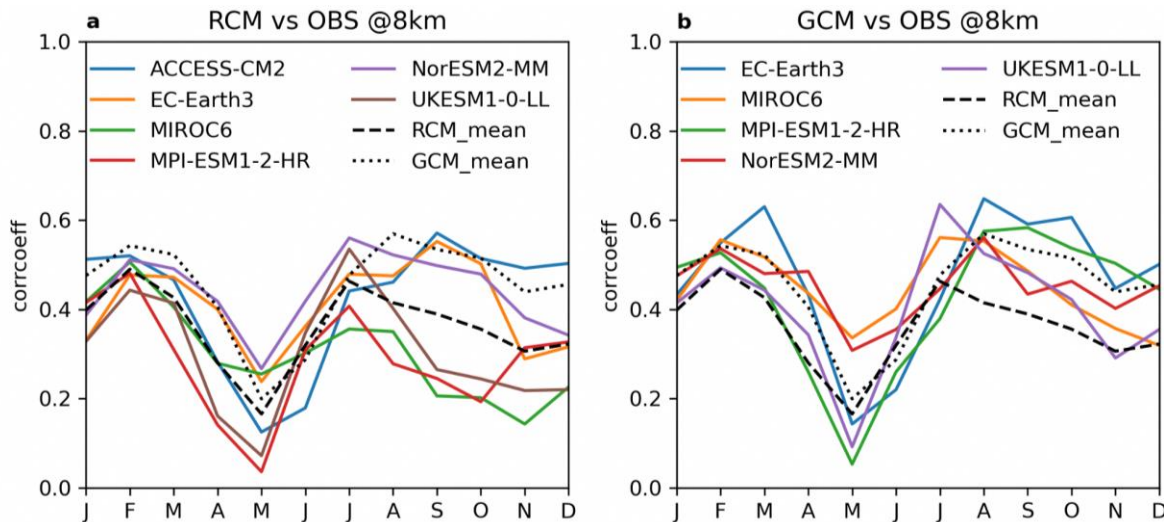

Figure 7.19: Correlation coefficient between the 8km observation and RCMs (a) or GCMs (b) over the MC region as to the ENSO teleconnection in the JJA season of the historical period (1995-2014).

7.6 Evaluation of local-scale climatology over Singapore

Assessment of regional scale climatology was presented in subchapter 7.4 above, which looked at the evaluation of key climate variables over the Maritime Continent in the 8 km downscaled simulations. In this subchapter we focus on the evaluation of 2 km downscaled simulations over Singapore. We have also carried out evaluation of the 8 km simulations over Singapore, but since the 2 km simulations are the primary dataset for the climate change projections over Singapore

presented in Chapter 10, we present the evaluation of the 2 km historical simulations in this chapter.

7.6.1 Mean Rainfall

The annual mean spatial pattern of precipitation over Singapore is shown in Figure 7.20. The mean precipitation values range from 0-10mm/day. The kriged precipitation over the Singapore land grids uses 28 observational stations with continuous data availability during the analysis period (1995-2014) Figure 7.20a. Please see Chapter 9 Section 9.7.1 for more information on the kriged rainfall.

The SINGV-RCM simulations at 2 km resolution forced by SINGV-RCM 8 km obtained from forcing ERA5 reanalysis is shown in Figure 7.20b and the multi-model annual pattern of mean precipitation simulated using 5 GCMs is shown in Figure 7.20c. The bias in the simulated annual mean precipitation with respect to station kriged precipitation are shown in Figure 7.20d, and e for downscaled data using ERA5 and multi-model mean, respectively.

The overall pattern of precipitation over the Singapore land grid points are well captured in the 2km model downscaled using ERA5 and multi-model mean with respect to the kriged precipitation mean.

The annual mean precipitation bias for ERA5 downscaled simulation (Figure 7.20d) shows dry bias over the central land grids and exhibits dry biases over the coastal grids of Singapore. This may be due to the fact that the model sees those grids as Ocean grid points. Also there is a slight overestimation of precipitation over the northernmost land grid points. MMM downscaled simulations (Figure 7.20e) shows similar low bias over the central land grids and exhibit dry biases over the coastal grids of Singapore, and we don't find the overestimation of precipitation over the northernmost land grid points.
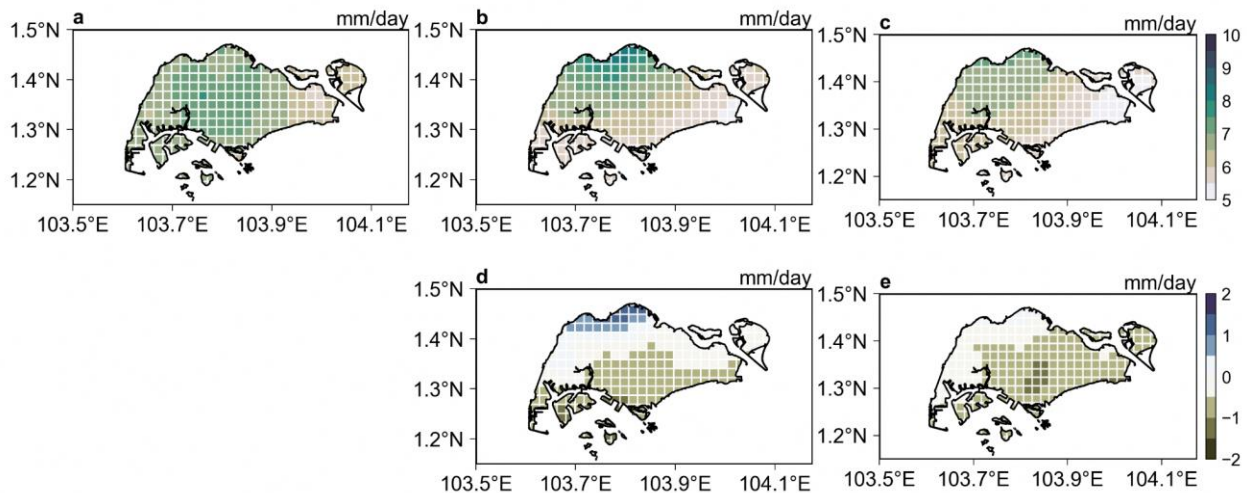

Figure 7.20: Annual mean precipitation in (a) Kriging gridded dataset, (b) ERA5 downscaled by SINGV (SINGV-ERA5) (c) Multimodel mean of downscaled GCM simulations with SINGV (SINGV-MMM). (d) shows the bias in SINGV-ERA5 (i.e. b -a), while (e) shows the bias in SINGV-MMM (i.e. c-a).

7.6.2 Rainfall Extremes

Extreme precipitation events are defined as the annual maximum daily maximum precipitation (Rx1day). The Annual RX1day spatial pattern of precipitation over Singapore is shown in Figure 7.21. The Annual RX1day in kriged precipitation ranges from 80 to 180 mm. There is a clear east-west contrast with east being wet and west being dry in the station observations Figure 7.21a.

The Annual RX1day of SINGV-RCM simulations at 2 km resolution from ERA5 is shown in figure 7.21b and the multi-model annual pattern of mean precipitation simulated using 5 GCMs is shown in Figure 7.21c.

The bias in the simulated Annual RX1day precipitation with respect to station kriged precipitation are shown in Figures 7.21d and 7.21e for downscaled using ERA5 and multi-model mean respectively. The Annual RX1day precipitation by 2km model downscaled using ERA5 shows upwards of 80mm in the grids over North-west of Singapore, while the 2km model downscaled using multi-model mean shows wet bias upwards of 80mm in grids over central-west land points of Singapore with respect to the kriged Annual RX1day precipitation.
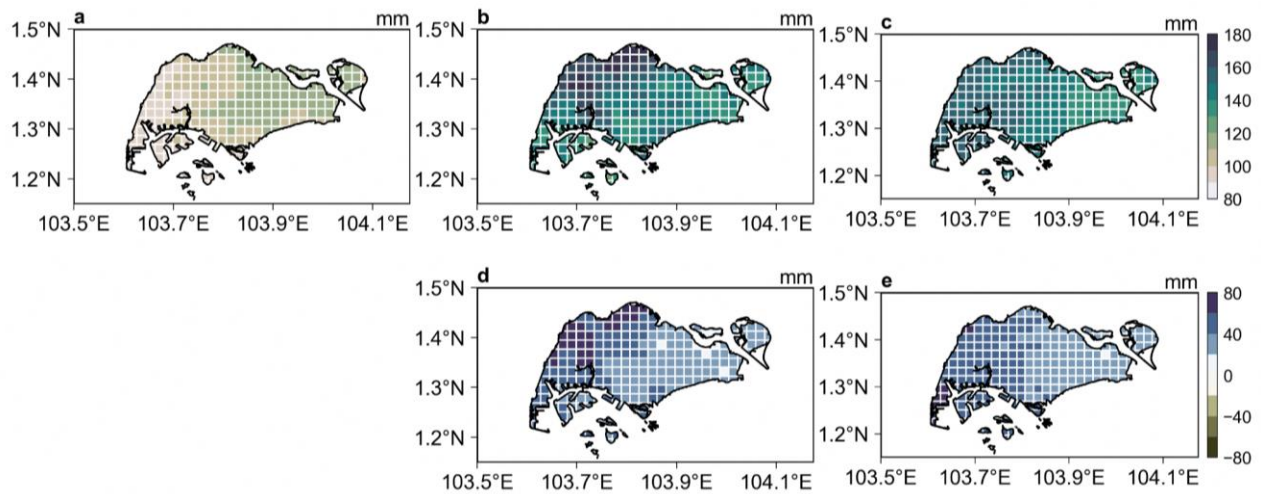
Figure 7.21: Annual RX1day in (a) kriged gridded dataset, (b) ERA5 downscaled by SINGV-RCM (SINGV-ERA5), (c) multimodel mean of downscaled GCM simulations with SINGV-RCM (SINGV-MMM). (d) Shows the bias in SINGV-ERA5 (i.e. b -a), while (e) shows the bias in SINGV-MMM (i.e. c-a).

7.6.3 Mean Temperature

The Annual spatial pattern of mean temperature over Singapore is shown in Figure 7.22. The mean annual temperature values range from 27-29 deg. Celsius.

The SINGV-RCM simulation of annual pattern of mean temperature at 2 km resolution forced by ERA5 reanalysis is shown in Figure 7.22a and the multi-model downscaled annual pattern of temperature simulated using 5 GCMs is shown in Figure 7.22b.

The overall pattern of annual Mean Temperatures over the Singapore land grid points are well captured in the 2km model downscaled using ERA5 and multi-model mean, with warm temperatures over the Central Business District (CBD) regions and cooler temperature over the less urbanized areas of North-West and Central regions.

Large warm biases are confined only over the coastal grid points and most grid points in the urbanized area are within the range of 0.1-0.3 deg. Celsius as shown in Figure 7.22c.

7.6.4 Temperature Extremes

Extreme Temperature events are defined as the highest maximum temperature (TXx) of the monthly maximum value of daily maximum temperature (TX). The Annual TXx spatial pattern of Temperature over Singapore is shown in Figure 7.23. The Annual TXx ranges from 30 to 38 deg. Celsius. The warmer temperature grids of above 36 deg. Celsius covers about 70-80% of Singapore land grid points in the ERA5 downscaled data as shown in Figure 7.23a.

The Annual TXx of SINGV-RCM simulations at 2 km resolution from ERA5 is shown in Figure 7.23a and the multi-model Annual TXx simulated using 5 GCMs is shown in Figure 7.23b.

The bias in the multi-model simulated (MMM) Annual TXx with respect to ERA5 downscaled data is shown in Figure 7.23c. The warm bias is between 1-2 deg. Celsius in the grids confined only over the northernmost land points and coastal land points of Singapore.
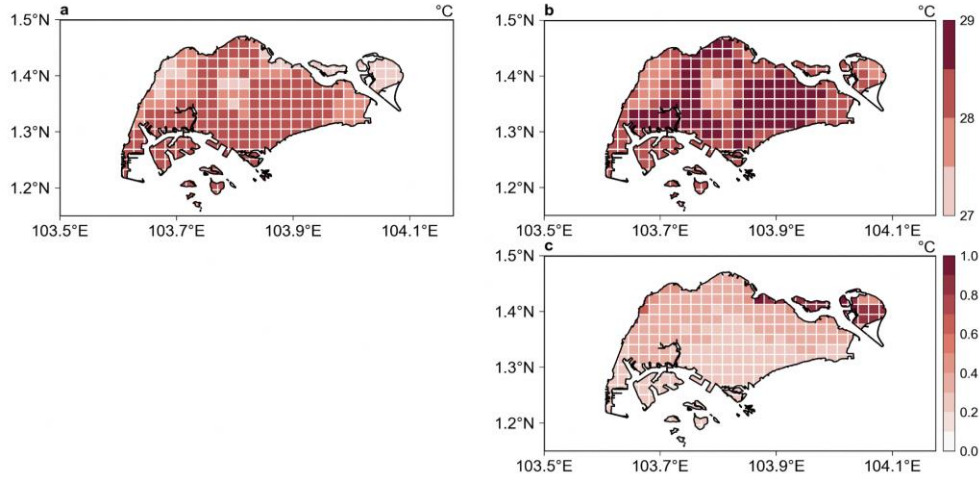
Figure 7.22: Annual mean temperature in (a) ERA5 downscaled by SINGV (SINGV-ERA5) (b) Multimodel mean of downscaled GCM simulations with SINGV (SINGV-MMM) and (c) shows the bias in SINGV-MMM relative to SINGV-ERA5 (i.e. b-a).
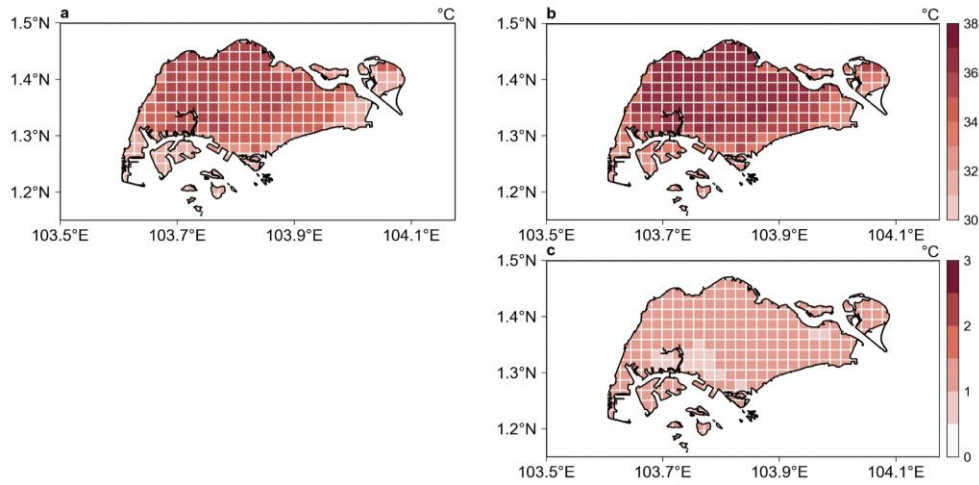

Figure 7.23: Annual TXx in (a) ERA5 downscaled by SINGV (SINGV-ERA5) (b) Multimodel mean of downscaled GCM simulations with SINGV (SINGV-MMM) and (c) shows the bias in SINGV-MMM relative to SINGV-ERA5 (i.e. b-a).
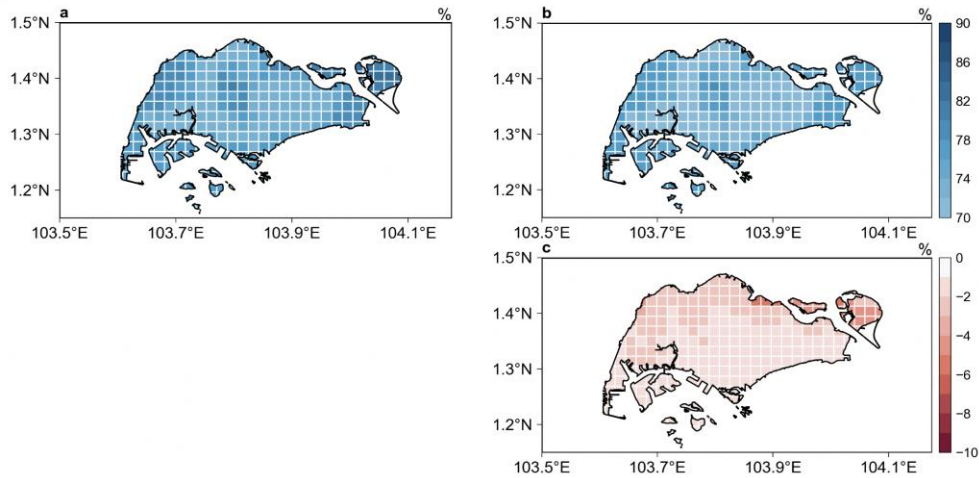

Figure 7.24: Annual mean relative humidity in (a) ERA5 downscaled by SINGV (SINGV-ERA5) (b) Multimodel mean of downscaled GCM simulations with SINGV (SINGV-MMM). (c) the bias in SINGV-MMM relative to SINGV-ERA5 (i.e. b -a).

7.6.5 Relative Humidity

The annual mean relative humidity over Singapore is shown in Figure 7.24. The mean relative values range from 70-90%, which is typical of a humid tropical location.

The SINGV-RCM simulations at 2 km resolution forced by SINGV-RCM 8 km obtained from forcing ERA5 reanalysis is shown in Figure 7.24a and the multi-model mean pattern of annual mean relative humidity simulated using 5 GCMs is shown in Figure 7.24b. The bias in the simulated annual mean relative humidity with respect to ERA5 downscaled dataset is shown in Figure 7.24c.

The annual mean relative humidity bias for MMM downscaled simulations (Figure 7.24c) shows negative bias over the east and west of central land grids and exhibits less biases over the southern coastal grids of Singapore.

7.6.6 Winds

The annual mean wind speed over Singapore is shown in Figure 7.25. The annual mean wind speed values range from 0-5 m/s.
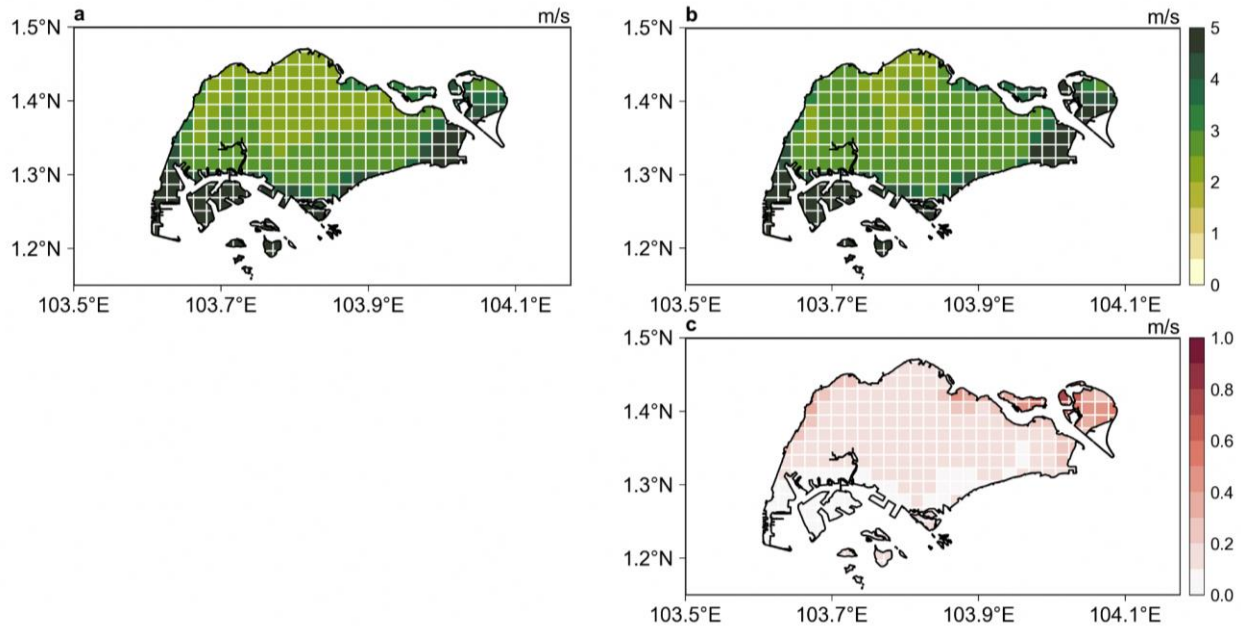

Figure 7.25: Annual mean wind speed in (a) ERA5 downscaled by SINGV (SINGV-ERA5) (b) Multimodel mean of downscaled GCM simulations with SINGV (SINGV-MMM). (c) the bias in SINGV-MMM relative to SINGV-ERA5 (i.e. b -a).

The SINGV-RCM simulations at 2 km resolution forced by SINGV-RCM 8 km obtained from forcing ERA5 reanalysis is shown in Figure 7.25a and the multi-model pattern of annual mean wind speed simulated using 5 GCMs is shown in Figure 7.25b. The bias in the simulated annual mean wind speed with respect to ERA5 downscaled dataset is shown in Figure 7.25c.

The annual mean wind speed bias for MMM downscaled simulations (Figure 7.25c) shows positive bias over the most of northern coastal grid points and exhibits less biases over the land grids of Singapore.

7.8 Summary

In summary, the downscaled simulations from ERA5 as well as 6 GCMs to 8 km resolution over South East Asia have shown added value in each variable compared to observations. Though the 2 km is not statistically different to 8 km over the western Maritime continent domain, to balance between very high computation costs and to benefit from high-resolution climate downscaling, we performed 2 km time slice simulations over the western Maritime continent domain in the historical as well as in the future for certain specific agency applications.

Following are some of the key summary points from this study:

1. We have clearly shown that there are added values in downscaling the coarse resolution driving models namely ERA-5 and 6 GCMs to 8 km and further to 2 km resolution.

2. We have clearly demonstrated the SINGV-RCM downscaling is consistent with the parent driving model and follows the long-term trends and variability of the parent driving model.

3. In this chapter, we evaluated the downscaled simulations of important meteorological parameters like precipitation, temperature, relative humidity as well as wind speed for different time scales of variability from diurnal to seasonal and their annual cycles are reproduced well in the model.

4. The important meteorological variables simulated by SINGV-RCM are compared with the available high-resolution regional observations like in situ (ground-based stations) and satellite merged products for establishing the model's skill in the historical period.

5. We have also brought out that the model is able to capture the regional climate drivers like remote teleconnection (ENSO-teleconnection) and processes like cold surges over this region by performing diagnostics with both observational data as well as simulated data.

6. Finally, the model is also evaluated over Singapore land grids using high resolution station observations in capturing the climate of the city state.

This chapter has documented the added value brought by the dynamical downscaling using SINGV-RCM to 8 km and 2 km resolution over SEA and WMC domains and the model's skill in capturing the different times scales of variability and also its ability to capture different regional processes. Further the usefulness of high-resolution 2km simulation in capturing the climate of a city state like Singapore is evident when compared with very high-resolution (both temporal as well as spatial) insitu station datasets.

References

Gelaro, R., and Coauthors, 2017: The Modern-Era Retrospective Analysis for Research and Applications, Version 2 (MERRA-2). J. Climate, 30, 5419–5454, https://doi.org/10.1175/JCLI-D-16-0758.1.

Hersbach, H, Bell, B, Berrisford, P, et al. The ERA5 global reanalysis. Q J R Meteorol Soc. 2020; 146: 1999– 2049. https://doi.org/10.1002/qj.3803.

Huffman, G.J.; Bolvin, D.T.; Braithwaite, D.; Hsu, K.; Joyce, R.; Kidd, C.; Nelkin, E.J.; Sorooshian, S.; Tan, J.; Xie, P. NASA Global Precipitation Measurement (GPM) Integrated Multi-satellitE Retrievals for GPM (IMERG). In Algorithm Theoretical Basis Document (ATBD) Version 06; NASA/GSFC: Greenbelt, MD, USA, 2019.

Huffman, George J., Bolvin, David T., Nelkin, Eric J., Wolff, David B., Adler, Robert F., Gu, Guojun, Hong, Yang, Bowman, Kenneth P., Stocker, Erich F.. 2007. The TRMM Multisatellite Precipitation Analysis (TMPA): Quasi-Global, Multiyear, Combined-Sensor Precipitation Estimates at Fine Scales. Journal of Hydrometeorology. Vol. 8, No. 1, pp. 38-55. DOI: 10.1175/JHM560.1 ISSN: 1525-755X, 1525-7541.

Morice, C. P., J. J. Kennedy, N. A. Rayner, and P. D. Jones (2012), Quantifying uncertainties in global and regional temperature change using an ensemble of observational estimates: The HadCRUT4 dataset, J. Geophys. Res., 117, D08101, doi:10.1029/2011JD017187.

Nguyen, P., E.J. Shearer, H. Tran, M. Ombadi, N. Hayatbini, T. Palacios, P. Huynh, G. Updegraff, K. Hsu, B. Kuligowski, W.S. Logan, and S. Sorooshian, The CHRS Data Portal, an easily accessible public repository for PERSIANN global satellite precipitation data, Nature Scientific Data, Vol. 6, Article 180296, 2019. doi: https://doi.org/10.1038/sdata.2018.296.

Roca, R., Alexander, L. V., Potter, G., Bador, M., Jucá, R., Contractor, S., Bosilovich, M. G., and Cloché, S.: FROGS: a daily 1° × 1° gridded precipitation database of rain gauge, satellite and reanalysis products, Earth Syst. Sci. Data, 11, 1017–1035, https://doi.org/10.5194/essd-11-1017-2019, 2019.

Rohde, R. A. and Hausfather, Z.: The Berkeley Earth Land/Ocean Temperature Record, Earth Syst. Sci. Data, 12, 3469–3479, https://doi.org/10.5194/essd-12-3469-2020, 2020.

Sadeghi, M., Nguyen, P., Naeini, M.R. et al. PERSIANN-CCS-CDR, a 3-hourly 0.04° global precipitation climate data record for heavy precipitation studies. Sci Data 8, 157 (2021). https://doi.org/10.1038/s41597-021-00940-9.

Shinya KOBAYASHI, Yukinari OTA, Yayoi HARADA, Ayataka EBITA, Masami MORIYA, Hirokatsu ONODA, Kazutoshi ONOGI, Hirotaka KAMAHORI, Chiaki KOBAYASHI, Hirokazu ENDO, Kengo MIYAOKA, Kiyotoshi TAKAHASHI, The JRA-55 Reanalysis: General Specifications and Basic Characteristics, Journal of the Meteorological Society of Japan. Ser. II, 2015, Volume 93, Issue 1, Pages 5-48, Released on J-STAGE March 18, 2015, Online ISSN 2186-9057, Print ISSN 0026-1165, https://doi.org/10.2151/jmsj.2015-001.

Torres-Alavez, J. A., F. Giorgi, F. Kucharski, E. Coppola, and L. Castro-García, 2021: ENSO teleconnections in an ensemble of CORDEX-CORE regional simulations. Clim. Dyn., 57, 1445–1461, https://doi.org/10.1007/s00382-020-05594-8.

Xie P, Joyce R, Wu S, Yoo S-H, Yarosh Y, Sun F and Lin R : 2017 Reprocessed, bias-corrected CMORPH global high-resolution precipitation estimates from 1998 J. Hydrometeorol. 18 1617–41.
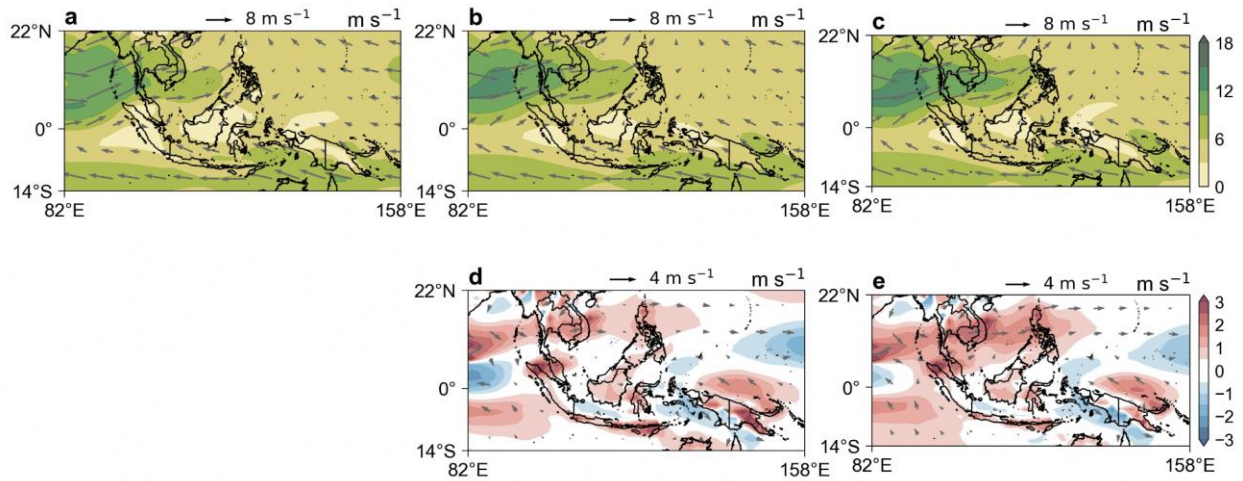
Appendix

Figure A7.1: Mean JJA 850 hPa winds (quivers) and wind speed (shaded) in (a) ERA5, (b) Mutimodel mean of 49 CMIP6 models, (c) Multimodel mean of GCMs used in downscaling. (d) shows the bias of the 49 CMIP6 models (i.e. b-a), while (e) shows the bias in the GCMs used in downscaling (i.e. c-a). Data in these plots have been regridded to 1.5x1.5 degrees.
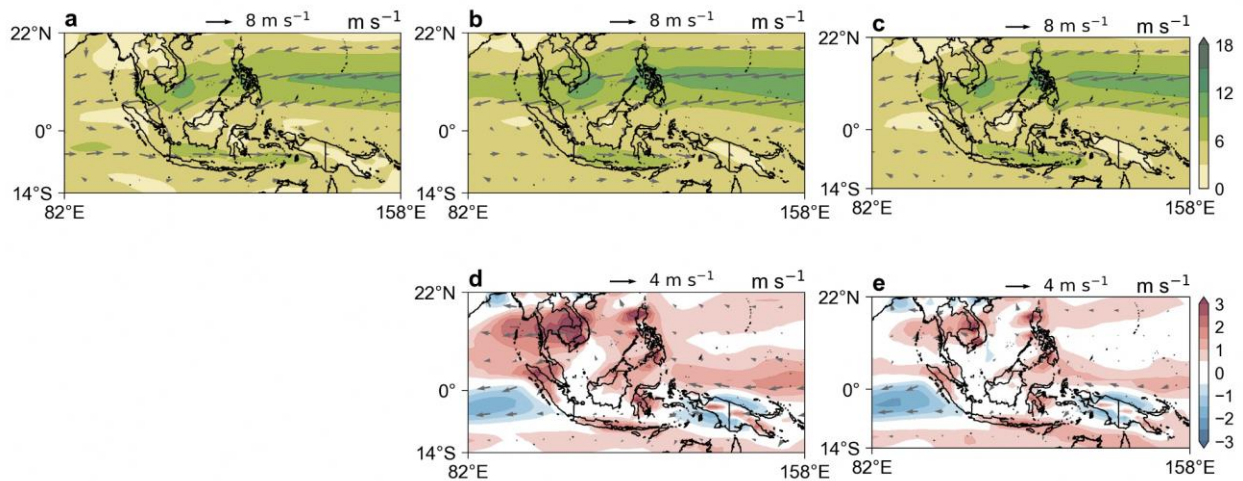

Figure A7.2: Mean DJF 850 hPa winds (quivers) and wind speed (shaded) in (a) ERA5, (b) Mutimodel mean of 49 CMIP6 models, (c) Multimodel mean of GCMs used in downscaling. (d) shows the bias of the 49 CMIP6 models (i.e. b-a), while (e) shows the bias in the GCMs used in downscaling (i.e. c-a). Data in these plots have been regridded to 1.5x1.5 degrees.